

Article

Comparison of Floating Offshore Wind Turbine Tower Deflection Mitigation Methods Using Nonlinear Optimal-Based Reduced-Stroke Tuned Vibration Absorber

Paweł Martynowicz ^{1,*} , Georgios M. Katsaounis ² and Spyridon A. Mavrakos ² ¹ Department of Process Control, AGH University of Krakow, Mickiewicza 30 Ave., 30-059 Kraków, Poland² School of Naval Architecture and Marine Engineering, National Technical University of Athens, 9, Iroon Polytechniou Str., 15772 Athens, Greece; katsage@mail.ntua.gr (G.M.K.); mavrakos@naval.ntua.gr (S.A.M.)

* Correspondence: pmartyn@agh.edu.pl

Abstract: Tower fatigue and strength are crucial operational concerns of floating offshore wind turbines (FOWTs) due to the escalation of the vibration phenomena observed on these structures as compared to land-based ones. FOWT towers are excited by wave and wind polyperiodic disturbances yielding continual transient states of structural vibration that are challenging for vibration mitigation systems. Thus, the paper investigates a novel implementation of nonlinear optimal-based vibration control solutions for the full-scale, tension leg platform (TLP)-based, NREL 5MW wind turbine tower-nacelle model with a 10-ton tuned vibration absorber (TVA), equipped with a magnetorheological (MR) damper, located at the nacelle. The structure is subjected to excessive wave and wind excitations, considering floating platform motions derived from model experiments in a wave tank. The MR damper operates simultaneously with an electromagnetic force actuator (forming a hybrid TVA) or independently (a semiactive TVA). The study includes both actuators' nonlinearities and dynamics, whereby the former are embedded in the Hamilton-principle-based nonlinear control solutions. The TVA is tuned either to the NREL 5MW tower-nacelle 1st bending mode frequency (*TVA-TN*) or to the TLP surge frequency (*TVA-TLP*). The optimal control task was redeveloped concerning the TVA stroke and transient vibration minimisation, including the implementation of the protected structure's acceleration and relative displacement terms, as well as the nonzero velocity term in the quality index. The regarded model is embedded in a *MATLAB/Simulink* environment. On the basis of the obtained results, the *TVA-TN* solution is by far superior to the *TVA-TLP* one. All the regarded *TVA-TN* solutions provide a tower deflection safety factor of ca. 2, while reference systems without any vibration reduction solutions or with a passive *TVA-TLP* are at risk of tower structural failure as well as the hybrid *TVA-TLP* system. The obtained TVA stroke reductions of 25.7%/22.0% coincide with 3.6%/10.3% maximum tower deflection reductions for the semiactive/hybrid *TVA-TN* case (respectively) with regard to the previously developed approaches. Moreover, these reductions are obtained due to the sole control algorithm enhancement; thus, no additional resources are necessary, while this attainment is accompanied by a reduction in the required MR damper force. The lowest obtained TVA stroke amplitude of 1.66 m is guaranteed by the newly introduced semiactive control. Its hybrid equivalent ensures 8% lower primary structure deflection amplitude and reduced nacelle acceleration levels thanks to the utilisation of the force actuator of the relatively low power (ca. 6 kW); the trade-off is an increased TVA stroke amplitude of 2.19 m, which, however, is the lowest among all the tested hybrid solutions. The analysed reference passive TVA systems, along with a modified ground-hook hybrid solution, can hardly be implemented in the nacelle (especially along the demanding side-side direction). The latter, being the well-proven hybrid solution for steady-state tower deflection minimisation, yielded unsatisfactory results. The achievements of the study may be used for an effective design of a full-scale vibration reduction system for the TLP-based floating wind turbine structure.

Keywords: floating offshore NREL 5MW wind turbine; tension leg platform; structural vibration; optimal-based control; hybrid tuned vibration absorber; magnetorheological damper



Citation: Martynowicz, P.; Katsaounis, G.M.; Mavrakos, S.A. Comparison of Floating Offshore Wind Turbine Tower Deflection Mitigation Methods Using Nonlinear Optimal-Based Reduced-Stroke Tuned Vibration Absorber. *Energies* **2024**, *17*, 1507. <https://doi.org/10.3390/en17061507>

Academic Editors:
Francesco Castellani and
Davide Astolfi

Received: 16 January 2024
Revised: 12 March 2024
Accepted: 14 March 2024
Published: 21 March 2024



Copyright: © 2024 by the authors. Licensee MDPI, Basel, Switzerland. This article is an open access article distributed under the terms and conditions of the Creative Commons Attribution (CC BY) license (<https://creativecommons.org/licenses/by/4.0/>).

1. Introduction

Slender structures such as beams, plates, towers, bridges [1], tall buildings [2], and wind turbines [3–5] suffer from mechanical vibrations, leading to increased fatigue and reduced life span. Most of these structures are fitted with dedicated solutions for vibration attenuation and fatigue reduction, such as tuned mass dampers/tuned vibration absorbers (TMDs/TVAs), tuned inerter dampers (TIDs), tuned liquid column dampers, bracing systems [6–10], etc. TVAs include an additional mass connected with the protected structure, usually by a spring and a damper, and possibly an actuator connected in parallel. TVAs are widely spread vibration reduction solutions. Depending on the damper and actuator type, passive, semi-active, active, and hybrid TVAs are used. The spring, damper, or actuator parameters are tuned to the selected vibration mode [11]. Passive TVAs cope reasonably with the vibration of a single frequency but cannot adapt to a broader excitation spectrum, a structure's frequency response variations, etc. [4]. Thus, advanced TVA solutions are used, among which TVAs utilising magnetorheological (MR) dampers (MR-TVAs) or the additional, small-scale active actuators (hybrid TVAs, H-TVAs, or hybrid MR-TVAs, H-MR-TVAs) gain an increasing interest [12–16]. The MR dampers are smart, semiactive actuators exhibiting wide resistance force ranges, millisecond response times, and high reliability, yet they suffer from a nonzero remanent force. Moreover, they cannot generate active forces, being semi-active devices [17–19]. The active force actuators of H-TVAs/H-MR-TVAs increase their vibration reduction efficiency; moreover, they provide greater robustness, eco-friendliness, and lower force/power requirements than active TVAs [20,21].

The paper focuses on the vibration control of a floating offshore wind turbine (FOWT) tower supported by a tension leg platform (TLP). The FOWT tower vibration arises due to both sea wave-induced platform motion and aerodynamic loads generated by wind, Karman vortices, variable inflow conditions for the blades, etc. Moreover, internal triggers such as imbalances in rotating machinery contribute to the tower's structural vibration and fatigue wear. Considering the type of turbine support, bottom-founded installations are used for water depths up to ca. 40–70 m, where their installation and operation can be economically feasible. For the challenge of expanding the offshore wind sector to greater depths, many types of floating concepts have been considered, such as spar buoys, barges, semisubmersibles, and tension leg platforms. Several pertinent designs have been completed; many scaled-down prototypes have been experimentally tested, whilst pilot full-scale developments have also been reported. Until 2021, 121.4 MW of floating wind energy was installed, with the majority (110.9 MW) in Europe and the remaining (10.5 MW) in Asia. The offshore wind sector is expanding, predicting 18.9 GW of new buildings by 2030 [22].

Spars have a simple construction composed of a single vertical cylinder, which forms the basis for installing the wind turbine tower. Spars are stabilised by ballast weight at the bottom of the cylinder and thus require deep water—their conventional mooring arrangement results in a large sea bed footprint. Spars are large structures requiring special building and equipment installation docking areas. Barges and semisubmersible platforms achieve stability through the large metacentric height obtained from the extended water plane area. Their design is a mature technology since it has been used in the oil and gas sector for many years. Barges and semi-subs do not require special docks for the building and can be towed relatively easily to the installation location. Their mooring arrangement usually follows a conventional design, resulting in a large sea bed footprint. Tension leg platforms usually consist of a submerged hull connected to vertical mooring lines (tendons). The hull's buoyancy is usually larger than the platform weight, resulting in a buoyancy surplus, which loads the tendons with a positive force (pretension). This pretension maintains the stability of the platform. The design of the buoyant part of the hull should ensure positive tendon forces in all operating and extreme conditions since compression in the tendons (which are usually made from steel pipes) results in buckling with catastrophic consequences. TLPs have a simple construction, which results in reduced manufacturing costs. Moreover, they can be installed in a wide range of water depths and

exhibit a small seabed footprint due to the vertical arrangement of the tendons. If their hull is similar to semi-subs, they do not require special equipment vessels for towing and installation. However, it should be noted that the TLP mooring system comprises a critical element for the strength of the whole structure, and it is usually expensive compared to conventional mooring arrangements. Additionally, the TLP concept makes the installation difficult in water areas with large tidal ranges.

Regarding the type of support structure, the conventional mooring arrangement of the spars, barges, and semisubmersibles permits significant linear and angular motions of the platforms due to the inherent low stiffness of the catenary-type mooring legs. In this respect, the tension leg concept offers the most stable solution, minimising the heave, pitch, and roll motions by imposing large pretension mooring forces. In this way, the platform is moving by the wave action mainly in the surge, and the wind turbine dynamics are comparatively less affected. Fatigue damage equivalent loads are lowest for TLP-based wind turbines [23]. TLP FOWT concepts combined with wave energy devices of the oscillating water column (OWC) type have been experimentally investigated in [24,25]. The surge response of a TLP FOWT combined with OWCs was measured in [24] and formed the basis for the vibration mitigation examined in the current study.

The problem of FOWT vibration control has been investigated many times within the last decade. The investigations concerned both structural fatigue and strength. The National Renewable Energy Laboratory (NREL) is one of the leading parties in this area, providing a systematic background for broader research (presented below) concerning the offshore version of NREL 5MW wind turbines [26,27]. In [28], a monopile, a barge, a spar buoy, and TLP wind turbine supports were investigated. A set of optimum passive TMDs was developed by building a limited degree-of-freedom model for each offshore wind support. The TMD parameters determined by the optimisation were applied to a series of wind turbine FAST SC simulations. A sensitivity analysis of the TMD parameters and a study on the effect of wind and wave misalignment on load reductions were also conducted. Tower fatigue damage reductions of up to 20% were achieved for the various TMD configurations. The results could have been even better if controlled vibration absorbers had been considered in this study. In [29,30], the impact of passive and semi-active pendulum-type TMD, located at the tower top, was analysed and simulated for both monopile and floating TLP-based GE Haliade 150–6MW wind turbines. Different control algorithms based on the on–off ground-hook policy were implemented, and the frequency responses were investigated. It was shown that the performance of each control policy depends on the load conditions. Fully coupled time domain analyses were conducted through the novel simulation tool integrated into the FASTv8 environment. Compared with the passive system, it was shown that the semi-active TMD results in higher load attenuation and smaller strokes under both the fatigue limit state and the ultimate limit state conditions. The ultimate loads at the tower base for the FOWT structure with semi-active TMD were increased by 3% for the shallow water depth and decreased by up to 9% for the deeper water. The clear limitation of this research was the simpleness and variable reliability of the assumed control algorithms. In [31], the nonlinear dynamic behaviour of the NREL 5MW wind turbine structure is evaluated considering various earthquake and wind intensities adopting a newly developed finite element model, which is first calibrated and verified using modal and static pushover analysis. This research shows that earthquake loads considerably inform the design and analysis of wind turbines. Moreover, the NREL 5MW tower failure conditions were established. The current work utilised these conditions to reference the obtained ultimate deflection amplitudes. One study [32] investigates a vibration control strategy for a barge-type FOWT by setting a stroke-limited H-TVA in the nacelle. The LQR active force controller is designed to reduce the vibration and loads of the wind turbine, and weighting coefficients are optimised considering the stroke of the H-TVA and the active control power. The developed controllers are deployed in high-fidelity simulations under typical wind and wave conditions. However, this approach suffers from force actuator dynamics not being included in the LQR formulation

(thus, the realised control output is not the same as the calculated one), while adding the stroke-limiting springs and dampers alters the TVA frequency at higher strokes. In [33], structural vibration control of an FOWT model with barge-type support is investigated. The system is equipped with MR-damper-based TVA located in the nacelle. Tower and barge rotational amplitude frequency responses are compared, proving the quality of the adopted optimal-based solutions and their potential to minimise the pitching amplitude of the structure (yielding wind energy extraction benefits) and MR damper force and/or stroke amplitude simultaneously. All of the actuator force nonlinearities are embedded in the control solution. Thus, the utilised approach is optimal or suboptimal for the assumed actuator, respecting its constraints. However, this research is limited to steady-state vibration analysis under monoharmonic rotor excitation of a relatively low (85 kN) amplitude. In [34], the numerical predictions of a TLP wind turbine response are discussed. The numerical model is calibrated vs. the physical test measurements. Open-FAST tools are used for hydrodynamic and motion response analyses. The TLP-based NREL 5MW FOWT model's dynamic response is compared with the physical model output concerning free-decay, regular and irregular wave tests, and analysed in time and frequency domains. This comparison addresses the uncertainties of the TLP wind turbine model, i.e., a 17% smaller natural period in surge extracted from the physical model compared to the numerical one, opening up a space for improvements. In [35], Madsen et al. covers the experimental testing of a TLP-based, pitch-regulated DTU 10 MW wind turbine at 1:60 scale in wind and waves. The responses of the floater to hydrodynamic loading are analysed and compared for two different feedback controllers: a typical onshore one tuned by a pole-placement technique and a floating wind turbine controller. Overall, the performance of the onshore controller results in a larger surge response than the offshore controller, leading to larger front mooring line tensions due to higher blade pitch angle amplitudes produced by the onshore controller. The shutdown cases of the offshore controller lead to larger surge displacement when the shutdown is initialised right before the wave impact as the aerodynamic damping is disabled. The research demonstrates the potential of physical model testing and numerical model validation. The experimental results of wind and wave alignment conditions influencing structural loads are used in this study as a reference. Larsen et al. [36] investigate an interesting use of a shunted electromagnetic transducer in a pendulum absorber to reduce tower vibration in monopile-supported wind turbines. An RCL network is designed as the supplemental shunt for the transducer's intrinsic RL properties, resulting in an additional resonance. The optimal system calibration is derived using the pole placement method. The shunted electromagnetic transducer operates as an equivalent mechanical spring-damper-inerter system (i.e., TID). The presented standard deviation results exhibit a slight advantage in vibration mitigation (0.14%/1.57% in fore-aft/side-side directions, respectively) of the electromagnetic transducer vs. the passive damper-based pendulum absorber; however, the benefits of the implementation of this active solution with all the necessary circuitry and power supply vs. the passive absorber are questionable.

Most of the vibration control solutions are based on the bang-bang control (ground-hook, sky-hook, sliding mode, etc.) [37,38], fuzzy logic, or two-stage approaches [1,17], which suffer from the inability to generate the force calculated in the first stage by the second-stage algorithm due to the actuator limitations, including force and stroke constraints, the inability to produce active forces, etc. The stroke constraints of the real-world vibration reduction system/TVA are frequently addressed by the use of end-stop collision bumpers or spring-damper buffer systems with stroke-dependent stiffness restoring force [32], which prevent the impact with the protected structure but, at the same time, deteriorate the vibration attenuation quality. Moreover, many first-stage algorithms require real-time vibration frequency determination, which is problematic for transient, polyperiodic, and multi-mode vibrations, for which these systems switch to the passive mode.

To address all the limitations mentioned above, a concept was devised to embed actuators' constraints into the control problem formulation [18–21] to avoid efficiency and

robustness problems of the calculated control function being imprecisely mapped or beyond the actuator output/TVA stroke limits. This involved the use of nonlinear control methods, which may be grouped generally as maximum-principle-based [39], Lyapunov-function-based [16,38], and linearisation-based methods utilising linear optimal control theory (LQR/LQG/ H_2/H_∞) [7,32,40,41]. The main implementation issues regarding these methods are the high computational load of the real-time operation or control quality degradation due to dynamics/disturbances that were unmodelled during offline pre-calculations. Thus, the concept of the maximum-principle-based nonlinear optimal-based vibration control was previously developed [18,19,21], eliminating all of the above computational or control authority problems.

The idea of simultaneous operation of the MR damper and the active force actuator was seldom investigated. Recently, it was literature-reviewed and implemented in a scaled laboratory model of an onshore wind turbine tower-nacelle structure with H-MR-TVA [21]. The developed concurrent MR damper–electric drive quasi-optimal and modified ground-hook control solutions provided significant attenuation of the steady-state monoharmonic vibration with regard to a passive system. The quasi-optimal control solution offered a significant energy efficiency advantage over the modified ground-hook law thanks to its various optimisation fields covered by the quality index; moreover, the MR damper and force actuator constraints were embedded in the optimal control task of the former, so they did not compromise the vibration control quality. No offline calculations nor disturbance assumptions were required for proper controller operation. The obtained results may be transferred to a full-scale real-world wind turbine structure thanks to the dynamical similarity [42].

Based on these results, the current research addresses the utilisation of the optimal-based, concurrent control algorithm for the TLP–NREL 5MW full-scale FOWT structure under excessive wave/wind conditions (characterised by polyperiodic excitations and continual transient vibration states), along with the design and tuning of the H-MR-TVA located in the nacelle; the optimal control task is enhanced with regard to the TVA stroke amplitude minimisation, including the implementation of the nacelle’s acceleration and relative displacement terms, as well as nonzero velocity term in the quality index, yielding the redeveloped optimal-based control propositions for both the MR damper current and the actuator force, being the main contributions of the paper. As a reference, the optimal-based, modified ground-hook law with the sole objective of the primary structure deflection minimisation is used along with the passive TVA system.

The paper is organised as follows. The succeeding section presents a regarded system. Next, the Pontryagin maximum-principle-based nonlinear optimal vibration control problem is stated and solved. Then, the numerical tests’ conditions, simulation model setup, and control implementation procedure are described. This is followed by the vibration control results and discussion. The paper is summed up with several conclusions.

2. A Regarded System

An NREL 5MW wind turbine (Table 1) tower-nacelle system, supported by a TLP [23] (Table 2), is regarded as a protected structure [26,27]. The NREL 5MW tower-nacelle system’s 1st bending mode corresponds to the dominant modal mass and vibration energy participation, especially for the low-frequency range associated with wave, wind and rotor excitations. Therefore, the current study takes into account the structure’s 1st bending mode modal parameters, such as mass m_1 , stiffness k_1 , and damping c_1 (Table 3). Previous studies confirm minor discrepancies of the 1 DOF tower-nacelle model vs. FAST code responses to tower base horizontal excitations [5,28], being the case regarded in the current research. An H-MR-TVA of the absorber mass m_2 and spring stiffness k_2 embedded in the nacelle is considered (Figure 1) based on [28]. The movement of both m_1 and m_2 is assumed to be linear displacement x_1 and x_2 , accordingly (small bending angles assumed), along the common, horizontal axis of an external force F_e (representing the resultant load applied to the nacelle i.a. through rotor) and the supporting TLP platform surge motion x_0 (Figure 1).

An MR damper and a small-scale electromagnetic actuator [21] of an output force F_a are both built-in parallel to the spring k_2 in the TVA system. The absorber stiffness k_2 (and damping c_2 for passive TVA tests) was tuned either to the NREL 5MW tower-nacelle 1st bending mode frequency of 0.30 Hz (from now on referred to as *TVA-TN*) or to the TLP surge frequency of 0.10 Hz (from now on referred to as *TVA-TLP*). For structural vibration control purposes, the MR damper was used, working in cooperation with the force actuator or independently.

Table 1. NREL 5MW baseline wind turbine parameters [26,28].

Rotor Diameter	126 m
Hub Height	90 m
Wind Speed: Cut-In, Rated, Cut-Out	3.0, 11.4, 25.0 m/s
Rotor Speed: Cut-In, Rated	6.9, 12.1 rpm
Rotor Mass	110.0 t
Nacelle Mass	240.0 t
Tower Mass	347.5 t
Nacelle Dimensions	18 × 6 × 6 m

Table 2. TLP platform main particulars [24].

Platform mass	2183 t
Displacement	6086.3 m ³
Vertical centre of gravity of the platform (below sea level)	4.05 m
Draft, Freeboard	20, 12 m
Nominal Tendon pretension (each)	10.8 MN
Water depth	120 m

Table 3. TLP–NREL 5MW with *TVA-TN*/*TVA-TLP* simulation model parameters.

NREL 5MW tower-nacelle 1st bending mode model	
m_1	428.8 t
k_1	1.546 MN/m
c_1	3.542 kNs/m
TVA tuned to NREL 5MW tower-nacelle 1st bending mode	
m_2	10.0 t (2.33% m_1)
k_2	34.42 kN/m
c_2	3.352 kNs/m
TVA tuned to TLP surge	
m_2	10.0 t (2.33% m_1)
k_2	3.770 kN/m
c_2	1.109 kNs/m

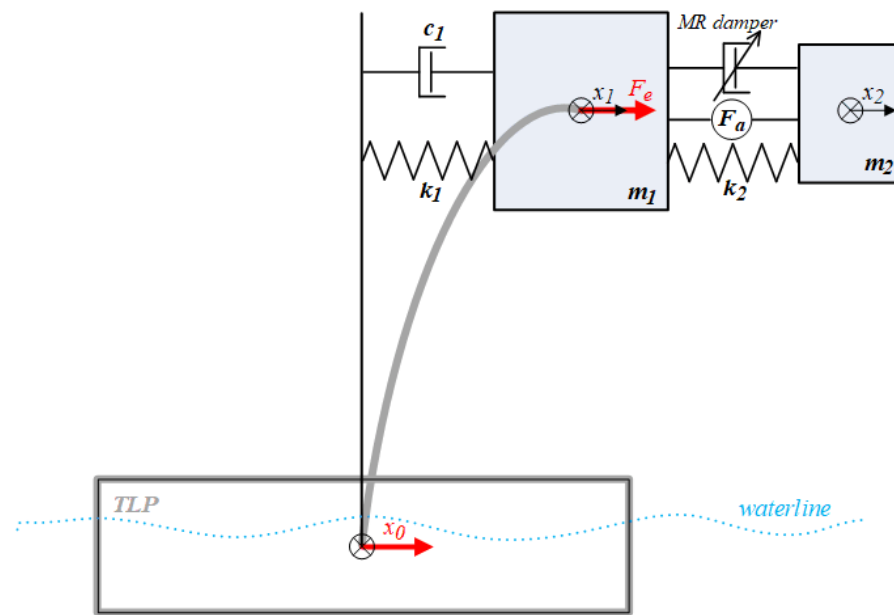


Figure 1. Diagram of a regarded system with an H-MR-TVA.

Tables 1 and 2 present the main particulars of the regarded FOWT structure. The values of the adopted simulation model parameters are given in Tables 3 and 4. The values of the m_1 , k_1 , and c_1 parameters were calculated on the basis of the 1st bending mode modal properties of the NREL 5MW tower-nacelle structure regarded as an Euler–Bernoulli cantilever beam with a tip mass [5], assuming m_1 to be the mass of the nacelle-rotor assembly enlarged by the 22.68% of the tower mass, based on the structural data given in [26–28,33]. The k_2 and c_2 values were selected using the Den Hartog principle [11] on the basis of the assumed tuning frequency and absorber mass $m_2 = 10$ t.

Table 4. MR damper simulation model parameters.

C_1	1581	N/A
C_2	38.25	N
C_3	12,240	Ns/Am
C_4	3570	Ns/m
ν	1300	s/m
p	1	1/s

Figure 2 presents bode diagrams of the regarded simulation model without TVA (*No TVA* legend) and with passive TVA tuned to the NREL 5MW tower-nacelle 1st bending mode (*TVA-TN* legend) concerning F_e input. The magnitude of the x_1 steady-state resonance vibration due to the passive TVA-TN implementation is reduced by 28.3 dB; however, the efficiency of the passive TVA along with MR-TVA, and H-MR-TVA will be investigated using random sea and wind state excitation patterns, enforcing continual transient vibration states, as described in Section 5.

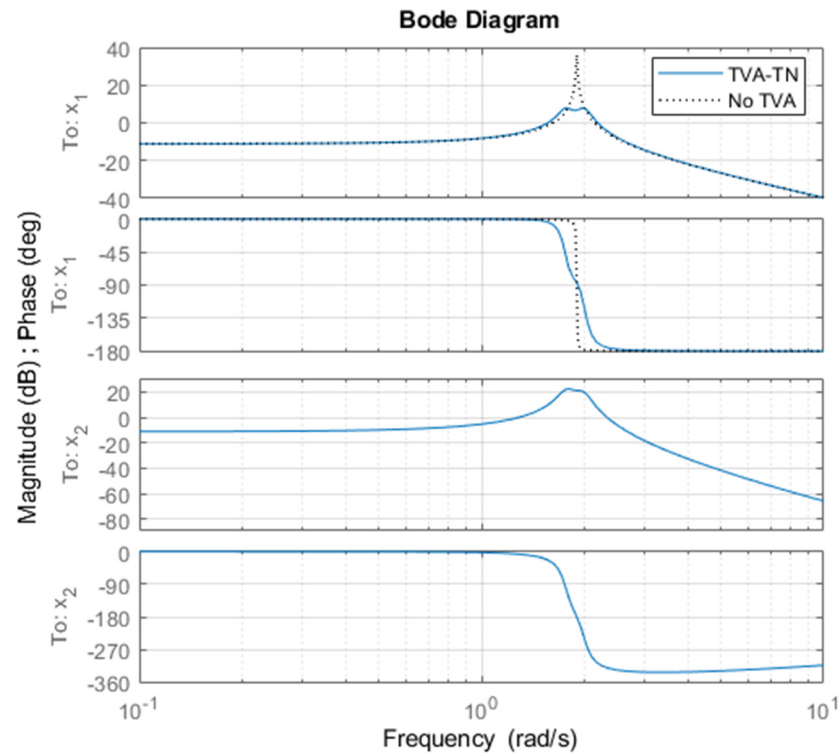


Figure 2. Bode diagram of a regarded simulation model with and without TVA.

3. Control Problem Formulation and Solution

The regarded system dynamics is described in a form of Equation (1):

$$\dot{z}(t) = f(z(t), u(t), t), t \in [t_0, t_1] \tag{1}$$

where $z(t)$ is a state vector:

$$z(t) = [z_1(t) \quad z_2(t) \quad z_3(t) \quad z_4(t)]^T, \tag{2}$$

while $u(t) = [u_1(t) \quad u_2(t)]^T \in U (U = R^2)$ is a piecewise-continuous control vector. A quality function to be minimised is:

$$G(z, u) = \int_{t_0}^{t_1} g(z(t), u(t), t) dt. \tag{3}$$

According to Figure 1, Section 2, let us assume: $z_1 = x_1, z_2 = \dot{x}_1, z_3 = x_2, z_4 = \dot{x}_2$, thus:

$$f(z, u, t) = \begin{bmatrix} z_2(t) \\ \frac{1}{m_1} (- (k_1 + k_2) z_1(t) - c_1 z_2(t) + k_2 z_3(t) + F_{mr}(z, u, t) + F_a(u, t) + k_1 x_0(t) + c_1 \dot{x}_0(t) + F_e(t)) \\ z_4(t) \\ \frac{1}{m_2} (k_2 z_1(t) - k_2 z_3(t) - F_{mr}(z, u, t) - F_a(u, t)) \end{bmatrix} \tag{4}$$

where:

$$F_{mr}(z, u, t) = (C_1 i_{mr}(u, t) + C_2) \tanh\{v[(z_4(t) - z_2(t)) + p(z_3(t) - z_1(t))]\} + (C_3 i_{mr}(u, t) + C_4)[(z_4(t) - z_2(t)) + p(z_3(t) - z_1(t))] \tag{5}$$

is the MR damper force as described in [18,33] with parameters tuned to the present application as given in Table 4; $i_{mr}(u)$ is the MR damper control current, $F_a(u)$ is the

actuator force [21], $F_e(t)$ is the nacelle horizontal excitation force, and $x_0(t)$ is the TLP surge that is assumed to be independent of the wind turbine tower-nacelle system bending in this research, as the NREL 5.0MW 1st tower bending modal mass is small in relation to the TLP structural mass plus an added mass due to the outgoing waves created by the floater motion [34]. The force produced by the MR damper includes electric current $i_{mr}(u, t)$ dependent friction force, viscous damping and stiffness components with a scaling parameter ν .

The MR damper current limitation to $[0, i_{max}]$ range ($i_{max} > 0$) and the actuator output nominal force limitation to $[-F_{nom}, F_{nom}]$ range were assumed as in [21]:

$$i_{mr}(u, t) = i_{max} \sin^2(u_1(t)), \tag{6}$$

$$F_a(u, t) = F_{nom} \sin(u_2(t)). \tag{7}$$

The regarded quality function (8) is:

$$g(z, u, t) = g_{11}(z_1(t) - x_0(t))^2 + g_{12}(z_2(t) - \dot{x}_0(t))^2 + g_{13}(z_1(t) - z_3(t))^2 + g_{14}(z_2(t) - z_4(t))^2 + g_{15}\dot{z}_2^2(t) + g_{21}i_{mr}^2(u, t) + g_{221}F_{mr}^2(z, u, t) + g_{222}F_a^2(u, t) + g_{23}P_a^2(z, u, t) \tag{8}$$

to account for the protected structure relative displacement (i.e., tower deflection) $z_1 - x_0$ and relative velocity (tower deflection rate) $z_2 - \dot{x}_0$ minimisation, the protected structure (nacelle) acceleration $\dot{z}_2 = \ddot{x}_1$ minimisation, the TVA stroke $z_1 - z_3$ and relative velocity $z_2 - z_4$ minimisation, the MR damper coil current i_{mr} and force F_{mr} minimisation, and the actuator force F_a and power P_a minimisation, where:

$$P_a(z, u, t) = F_a(u, t)(z_2(t) - z_4(t)), \tag{9}$$

$$\dot{z}_2(t) = \frac{1}{m_1}(- (k_1 + k_2)z_1(t) - c_1z_2(t) + k_2z_3(t) + F_{mr}(z, u, t) + F_a(u, t) + k_1x_0(t) + c_1\dot{x}_0(t) + F_e(t)).$$

The newly introduced term $g_{15}\dot{z}_2^2(t)$ implementation, the original contribution of current research, is intended to minimise the protected structure’s (i.e., nacelle/rotor with its sensitive instrumentation) acceleration. As the structure acceleration increases with the square of the frequency (for the constant oscillation displacement amplitude), this term is aimed to minimise predominantly higher frequency content of the displacement x_1 (thus minimising the acceleration \ddot{x}_1). At these higher frequencies TVA mass vibrates at a close antiphase to the protected structure’s mass—see x_1 vs. x_2 phase diagrams (Figure 2). Thus, the minimisation of the high-frequency content of x_1 with the use of appropriate g_{15} weight consequently reduces moving away the protected structure and the TVA (due to the close antiphase). This, in turn, reduces the TVA stroke amplitude and MR damper force amplitude, which will be proven in Section 7.

Let us consider the Hamiltonian in a form (10):

$$H(\xi, z, u, t) = -g(z, u, t) + \xi^T(t)f(z, u, t). \tag{10}$$

If (z^*, u^*) pair is an optimal control process, there exists an adjoint vector function ξ satisfying:

$$\dot{\xi}(t) = -f_z^{*T}(z^*, u^*, t)\xi(t) + g_z^T(z^*, u^*, t), t \in [t_0, t_1] \tag{11}$$

with a transversality condition:

$$\xi(t_1) = 0 \tag{12}$$

so that $u^*(t)$ maximises the Hamiltonian over the set U for almost all $t \in [t_0, t_1]$ (see details in [43]). For the regarded system, the adjoint (co-state) vector is:

$$\xi(t) = [\xi_1(t) \quad \xi_2(t) \quad \xi_3(t) \quad \xi_4(t)]^T, \tag{13}$$

whereas:

$$f_z^{*T}(z^*, u^*, t) = \begin{bmatrix} 0 & -\frac{1}{m_1} \left(k_1 + k_2 + p\tilde{F}_{mr}(z^*, u^*, t) \right) & 0 & \frac{1}{m_2} \left(k_2 + p\tilde{F}_{mr}(z^*, u^*, t) \right) \\ 1 & -\frac{1}{m_1} \left(c_1 + \tilde{F}_{mr}(z^*, u^*, t) \right) & 0 & \frac{1}{m_2} \left(\tilde{F}_{mr}(z^*, u^*, t) \right) \\ 0 & \frac{1}{m_1} \left(k_2 + p\tilde{F}_{mr}(z^*, u^*, t) \right) & 0 & -\frac{1}{m_2} \left(k_2 + p\tilde{F}_{mr}(z^*, u^*, t) \right) \\ 0 & \frac{1}{m_1} \left(\tilde{F}_{mr}(z^*, u^*, t) \right) & 1 & -\frac{1}{m_2} \left(\tilde{F}_{mr}(z^*, u^*, t) \right) \end{bmatrix} \quad (14)$$

and:

$$g_z^T(z^*, u^*, t) = \begin{bmatrix} 2g_{11}(z_1^*(t) - x_0(t)) + 2g_{13}(z_1^*(t) - z_3^*(t)) - 2g_{221}pF'_{mr}(z^*, u^*, t) - \frac{2g_{15}}{m_1}z_2^*(t) \left(k_1 + k_2 + p\tilde{F}_{mr}(z^*, u^*, t) \right) \\ 2g_{12}(z_2^*(t) - \dot{x}_0(t)) + 2g_{14}(z_2^*(t) - z_4^*(t)) - 2g_{221}F'_{mr}(z^*, u^*, t) + 2g_{23}F_a^2(u^*)(z_2^*(t) - z_4^*(t)) - \frac{2g_{15}}{m_1}z_2^*(t) \left(c_1 + \tilde{F}_{mr}(z^*, u^*, t) \right) \\ -2g_{13}(z_1^*(t) - z_3^*(t)) + 2g_{221}pF'_{mr}(z^*, u^*, t) + \frac{2g_{15}}{m_1}z_2^*(t) \left(k_2 + p\tilde{F}_{mr}(z^*, u^*, t) \right) \\ -2g_{14}(z_2^*(t) - z_4^*(t)) + 2g_{221}F'_{mr}(z^*, u^*, t) - 2g_{23}F_a^2(u^*)(z_2^*(t) - z_4^*(t)) + \frac{2g_{15}}{m_1}z_2^*(t)\tilde{F}_{mr}(z^*, u^*, t) \end{bmatrix} \quad (15)$$

with:

$$\tilde{F}_{mr}(z^*, u^*, t) = \nu(C_1 i_{mr}(u^*, t) + C_2) \left\{ 1 - \tanh^2[\nu(z_4^*(t) + pz_3^*(t) - z_2^*(t) - pz_1^*(t))] \right\} + (C_3 i_{mr}(u^*, t) + C_4),$$

$$F'_{mr}(z^*, u^*, t) = F_{mr}(z^*, u^*, t)\tilde{F}_{mr}(z^*, u^*, t).$$

The Hamiltonian therefore takes the form (16):

$$H(\xi, z, u, t) = -g_{11}(z_1(t) - x_0(t))^2 - g_{12}(z_2(t) - \dot{x}_0(t))^2 - g_{13}(z_1(t) - z_3(t))^2 - g_{14}(z_2(t) - z_4(t))^2 - g_{15}\dot{z}_2^2(t) - g_{21}i_{mr}^2(u, t) - g_{221}F_{mr}^2(z, u, t) - g_{222}F_a^2(u, t) - g_{23}F_a^2(u, t)(z_2(t) - z_4(t))^2 + \xi^T(t)f(z, u, t). \quad (16)$$

The Hamiltonian maximisation conditions [43] are:

$$\frac{\partial H(\xi, z, u, t)}{\partial u_1(t)} = \left\{ \left(\frac{1}{m_1}\xi_2(t) - \frac{1}{m_2}\xi_4(t) - 2g_{221}F_{mr}(z, u, t) - \frac{2g_{15}}{m_1}\dot{z}_2(t) \right) \frac{\partial F_{mr}(z, u, t)}{\partial i_{mr}(u, t)} - 2i_{max}g_{21}\sin^2(u_1(t)) \right\} \sin(2u_1(t))i_{max} = 0 \quad (17)$$

$$\frac{\partial H(\xi, z, u, t)}{\partial u_2(t)} = \left\{ \frac{1}{m_1}\xi_2(t) - \frac{1}{m_2}\xi_4(t) - \frac{2g_{15}}{m_1}\dot{z}_2(t) - 2F_{nom} \left[g_{222} + g_{23}(z_2(t) - z_4(t))^2 \right] \sin(u_2(t)) \right\} \cos(u_2(t))F_{nom} = 0 \quad (18)$$

with the appropriate sign change conditions, where:

$$\frac{\partial F_{mr}(z, u, t)}{\partial i_{mr}(u, t)} = C_1 \tanh[\nu(z_4(t) + pz_3(t) - z_2(t) - pz_1(t))] + C_3(z_4(t) + pz_3(t) - z_2(t) - pz_1(t))$$

Fixing an attention on $[0, \pi)$ range of $u_1(t)$, Equation (17) results in ($g_{21} \neq 0$):

$$\sin(2u_1(t)) = 0 \quad (19)$$

or:

$$\sin^2(u_1(t)) = \frac{1}{2i_{max}g_{21}} \left(\frac{1}{m_1}\xi_2(t) - \frac{1}{m_2}\xi_4(t) - \frac{2g_{15}}{m_1}\dot{z}_2(t) - 2g_{221}F_{mr}(z, u, t) \right) \frac{\partial F_{mr}(z, u, t)}{\partial i_{mr}(u, t)} \quad (20)$$

Analogically to [19]:

$$i_{mr}^*(u^*, t) = \begin{cases} 0, & \text{if } RHS(20) < 0 \\ \frac{1}{2g_{21}} \left(\frac{1}{m_1} \zeta_2(t) - \frac{1}{m_2} \zeta_4(t) - \frac{2g_{15}}{m_1} \dot{z}_2(t) - 2g_{221} F_{mr}(z, u, t) \right) \frac{\partial F_{mr}(z, u, t)}{\partial i_{mr}(u, t)}, & \text{if } RHS(20) \in [0, 1) \\ i_{max}, & \text{if } RHS(20) \geq 1 \end{cases} \quad (21)$$

where $RHS(20)$ is the right-hand side of Equation (20).

From condition (18) we obtain ($g_{222} \neq 0$):

$$\frac{\partial H(\xi, z, u, t)}{\partial u_2(t)} = \left\{ \frac{1}{2F_{nom} [g_{222} + g_{23}(z_2(t) - z_4(t))^2]} \left(\frac{1}{m_1} \zeta_2(t) - \frac{1}{m_2} \zeta_4(t) - \frac{2g_{15}}{m_1} \dot{z}_2(t) \right) - \sin(u_2(t)) \right\} \cos(u_2(t)) = 0 \quad (22)$$

Fixing an attention on $[-\pi, \pi]$ range of $u_2(t)$, Equation (22) results in proposition (23)–(25), analogically to [21]:

1. *if* $\left\{ \frac{1}{2F_{nom} [g_{222} + g_{23}(z_2(t) - z_4(t))^2]} \left(\frac{1}{m_1} \zeta_2(t) - \frac{1}{m_2} \zeta_4(t) - \frac{2g_{15}}{m_1} \dot{z}_2(t) \right) \right\} \leq -1$, *then* (22) is fulfilled and $\frac{\partial H(\xi, z, u, t)}{\partial u_2(t)}$ exhibits +/− sign change (Hamiltonian maximisation) for: $u_2^*(t) = -\frac{\pi}{2}$ only; thus:

$$F_a^*(u^*, t) = -F_{nom}. \quad (23)$$

2. *if* $\left\{ \frac{1}{2F_{nom} [g_{222} + g_{23}(z_2(t) - z_4(t))^2]} \left(\frac{1}{m_1} \zeta_2(t) - \frac{1}{m_2} \zeta_4(t) - \frac{2g_{15}}{m_1} \dot{z}_2(t) \right) \right\} \geq 1$, *then* (22) is fulfilled and $\frac{\partial H(\xi, z, u, t)}{\partial u_2(t)}$ exhibits +/− sign change for: $u_2^*(t) = \frac{\pi}{2}$ only; thus:

$$F_a^*(u^*, t) = F_{nom}. \quad (24)$$

3. *if* $\left\{ \frac{1}{2F_{nom} [g_{222} + g_{23}(z_2(t) - z_4(t))^2]} \left(\frac{1}{m_1} \zeta_2(t) - \frac{1}{m_2} \zeta_4(t) - \frac{2g_{15}}{m_1} \dot{z}_2(t) \right) \right\} \in (-1, 1)$, *then* (2) is fulfilled and $\frac{\partial H(\xi, z, u, t)}{\partial u_2(t)}$ exhibits +/− sign change for: $u_2^*(t) = \arcsin \left\{ \frac{1}{2F_{nom} [g_{222} + g_{23}(z_2^*(t) - z_4^*(t))^2]} \left(\frac{1}{m_1} \zeta_2(t) - \frac{1}{m_2} \zeta_4(t) - \frac{2g_{15}}{m_1} \dot{z}_2(t) \right) \right\}$ only; thus:

$$F_a^*(u^*, t) = \frac{1}{2 [g_{222} + g_{23}(z_2^*(t) - z_4^*(t))^2]} \left(\frac{1}{m_1} \zeta_2(t) - \frac{1}{m_2} \zeta_4(t) \right). \quad (25)$$

4. Test Conditions

The TLP surge $x_0(t)$ realisations used in this research correspond to the platform’s response under the action of an ocean wave spectrum of the Bretschneider type. The examined TLP platform is shown in Figures 3 and 4. It has a triangular arrangement and is composed of vertical buoyant cylinders interconnected with cylindrical bracing members. Three of the vertical cylinders are placed at the vertices of the triangle providing the major part of the buoyancy. A 5MW NREL offshore wind turbine is installed on a cylinder at the centre of the triangle. The concept includes also devices for parallel wave energy extraction of the oscillating water column type (OWC). Their air chambers are formed by a concentric skirt and a dome, which surround each cylinder at the vertices of the triangle.

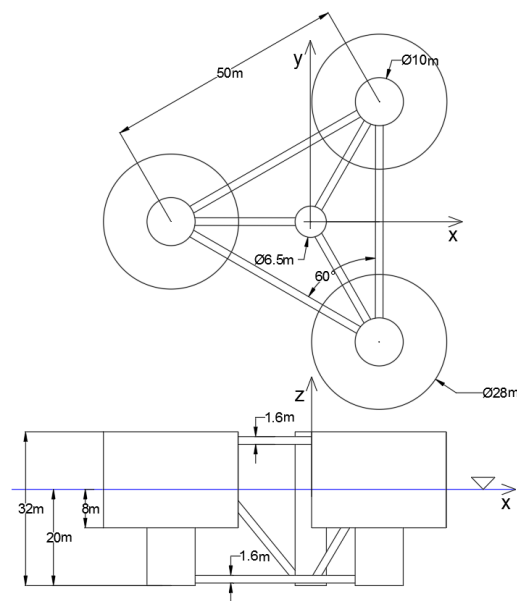


Figure 3. TLP platform dimensions.

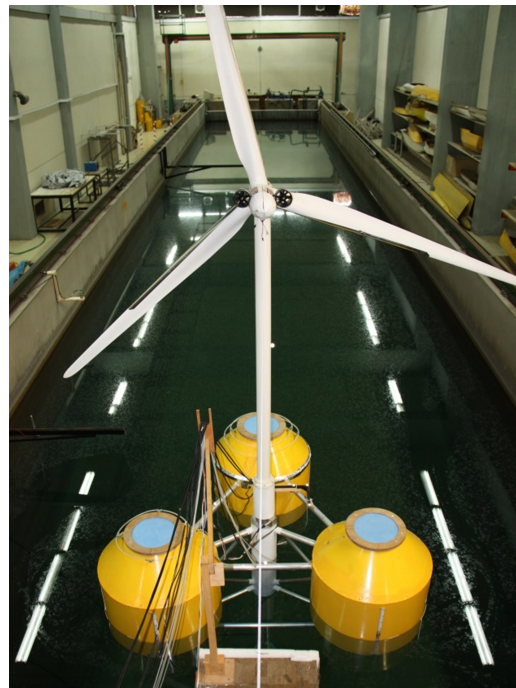


Figure 4. TLP with NREL 5MW model in the experimental facilities.

The platform is moored to the sea bed using tensioned legs, placed vertically between the corner cylinders and the sea bottom. The floating cylinders provide a substantial buoyancy surplus, generating the necessary pretension in the mooring tendons for platform stabilisation and station keeping.

A breakdown of the platform weight groups is presented in Table 2, together with the tendon loads. The experimental investigation of the dynamic behaviour of the floating platform was carried out in the wave basin of the National Technical University of Athens (NTUA) using the scaled-down instrumented model (scale 1:40) shown in Figure 4.

The sea wave actions were simulated following the Froude law of scaling, which ensures the dynamic similarity to the prototype by preserving the ratio of the inertial to the gravitational forces. The experiments included both monochromatic waves and

random sea states. Their parameters (periods and amplitudes) were selected from a wide range, corresponding to the wave climates prevailing in the candidate installation location (Aegean Sea). Figure 5 depicts the measured surge response amplitude operators, RAOs (i.e., motion amplitude in the surge due to a harmonic wave of unit amplitude).

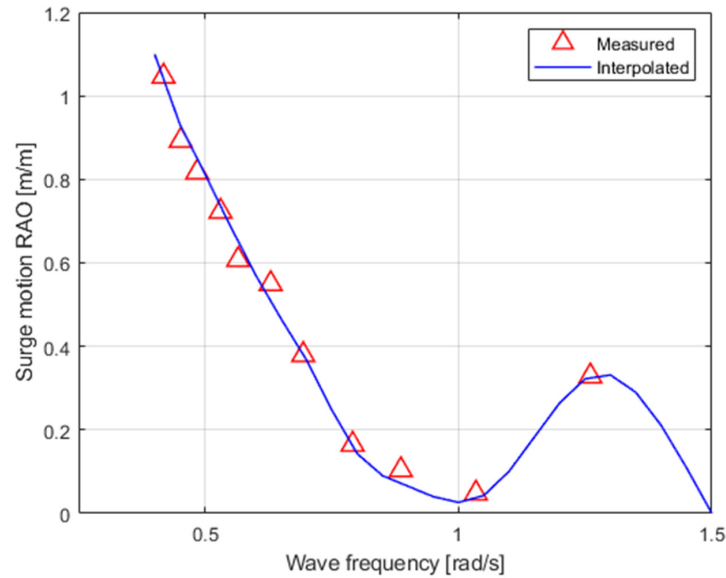


Figure 5. Surge motion RAOs for the TLP FOWT.

For the installation location considered in the Aegean Sea, the most probable severe wave state can be described by a Bretschneider wave spectrum $S(\omega)$ (Figure 6) having a significant wave height of 4 m and a peak period of 8.3 s. The corresponding spectrum of the surge response (26) can be found through the combination of the sea wave spectrum and the surge motion RAOs:

$$S_{surge}(\omega) = S(\omega)RAO^2(\omega) \tag{26}$$

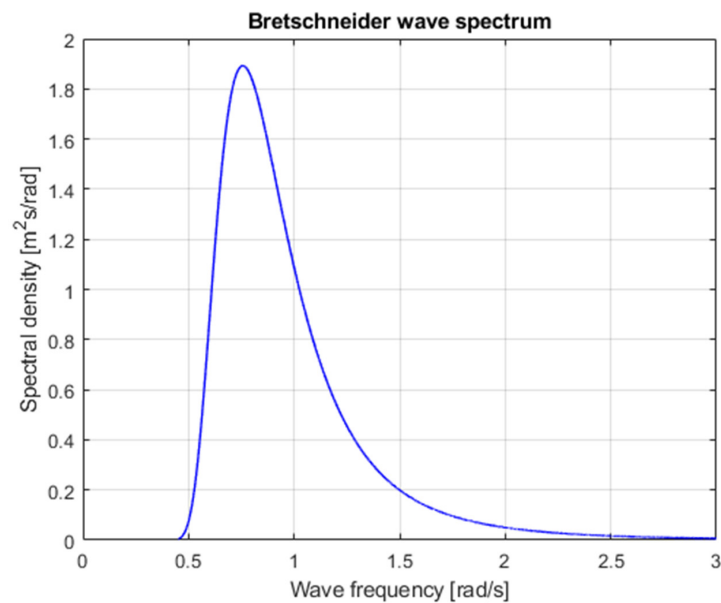


Figure 6. Wave spectrum considered.

Based on the experimentally derived platform surge spectrum, ten random realizations (numbered 0 through 9) of surge motion were produced by combining the spectral density and random phases for individual motion components.

The external excitation applied on the tower-nacelle structure through the rotor is mainly due to changeable aerodynamic loads. The wind realisations at 90 m above the open sea level were generated using the Weibull distribution with a scale parameter of 10 and shape parameter of 2.0, resulting in 8.86 m/s mean wind speed and 4.63 m/s standard deviation. The horizontal nacelle excitation force $F_e(t)$ was then calculated using the rotor thrust data from the characteristics of ‘Steady-state responses as a function of wind speed’ [26], which is generally consistent with [44].

The most severe vibration excitation case of coaxial wind and wave loads was assumed. Ten Bredsnieder spectrum ocean wave realisations $0 \div 9$ were paired with ten Weibull distribution wind patterns $0 \div 9$, 2500 s in length each, 1 ms of time resolution, as described above. Due to a continual thrust asymmetry for all the 360° rotor angular positions but six ones (i.e., 0° , 60° , 120° , 180° , 240° , 300°) corresponding to one of the blades being aligned with the tower, both tower fore–aft and side–side bending mode is excited. Moreover, TLP horizontal excitation directions (surge/sway) may vary, too. Current analyses assume (H-)MR-TVA operation direction as the excitation direction. In a practical implementation, two (H-)MR-TVAs operating along mutually perpendicular directions (side–side/fore–aft) may be installed, or a single (H-)MR-TVA operating along the side–side direction (fore–aft vibrations attenuated by the rotor aerodynamic damping and collective pitch control of the blades). The assumed here excitation combinations, including their alignment, are not necessarily frequent in real-world conditions. The analyses of the wave/wind misalignment [28] suggest that side–side TVA installation is necessary due to side–side loads being a large contributor to the overall fatigue wear and ultimate fracture risk. The work [35] indicates that the aerodynamic damping is strongest on the surge motion for unidirectional conditions; thus, a fore–aft TVA may also be essential for wave/wind misalignment.

5. Simulation Setup

The NREL 5MW tower-nacelle 1st bending mode model equipped with passive TVA/MR-TVA/H-MR-TVA located in the nacelle, excited horizontally by the supporting TLP platform surge x_0 and resultant load applied to the nacelle F_e , was embedded in *MATLAB/Simulink* environment, adopting the fixed $t_s = 1$ ms sampling step. A relatively low TVA mass m_2 of 10 tons (0.35% of the total structure’s mass) was assumed, yielding a 2.33% m_2/m_1 mass ratio, regarding 1st bending mode mass m_1 of 428.8 tons. As discussed earlier [21], an increased TVA mass ratio does not yield a proportional efficiency gain, not to mention the spatial and structural support requirements; however, it contributes to lower TVA sensitivity to detuning [45] and more limited TVA stroke. The selection of the 10-ton absorber mass is consistent with [28]. Therefore, the current study discusses the benefits of implementing an MR damper (and possibly a small-scale force actuator) to address all the regarded efficiency, stroke/space/structural support limitations and detuning issues, using a smaller absorber mass.

In addition to the MR damper’s and actuator’s static non-linearities discussed above (5)–(7), their linear dynamics (27) and (28) are also included in the current study:

$$G_{mr}(s) = \frac{F_{mr}^{act}(s)}{F_{mr}(s)} = \frac{1}{0.0051s + 1} e^{-0.0029s}, \quad (27)$$

$$G_a(s) = \frac{F_a^{act}(s)}{F_a(s)} = \frac{32.6s^2 + 1.55e4s + 9.66e4}{s^3 + 140s^2 + 1.71e4s + 1.06e5} e^{-0.0060s}, \quad (28)$$

where $F_{mr}^{act}(s)$ and $F_a^{act}(s)$ are Laplace transforms of actual MR damper and electromagnetic actuator outputs, respectively. However, as the MR damper dynamics (27) may be modelled with a 2nd order inertia, while the electromagnetic actuator time-delayed transfer function

(28) [21] may be modelled with a 2nd order oscillatory dynamics with a 1st order inertia, the corresponding optimal control task would be of the 9th order. This would yield a computational load that was real-time tested to be unrealisable. Thus, the dynamics of the MR damper and the electromagnetic actuator are both embedded in the simulation model of the NREL 5MW tower-nacelle system equipped with a TVA, supported by the TLP; the actual values of F_{mr}^{act}/F_a^{act} are fed as F_{mr}/F_a into Equations (4), (8), (11), (21) and (23)–(25) (in this way, the modelled MR damper and force actuator responses inertia and delays influence state and co-state variables' values as well as i_{mr}^* and F_a^* control patterns), but they do not augment optimal problem order. This guarantees the simplicity of the real-time implementation, while not impairing the overall system performance (partially due to the frequency spectrum of the regarded vibration problem being low in relation to actuators' dynamics).

All the structural model parameters, as in Table 3, along with the MR damper model parameters (Table 4) were assumed for the simulations. The value of $i_{max} = 1$ A yielding respective F_{mr} ranges and nominal actuator output force $F_{nom} = 7.125$ kN were tuned to the current application. As previously proven [21], the MR damper responds faster than the electromagnetic actuator. In contrast, the actuator may cancel the MR damper undesirable (i.e., of improper sign due to its dissipative nature) force. The resultant maximum MR damper force was ca. 50 kN (excluding the more demanding *Mod.GH* and *Mod.GH-H* solutions), whereas the mean actuator power was up to 6.27 kW for *TVA-TN* hybrid solutions; however, less force/power demanding solutions were investigated as well.

6. Control Implementation

For the vibration control of the FOWT 1st bending mode, the approach described in Sections 3 and 5 was implemented using the MR damper control Formula (21) and the force actuator control Formula (23)–(25). Regarding the considerations presented in [18–21], the control propositions (21) and (23)–(25) were implemented using the optimisation horizon equal to one integration step [18,21]; as it was proven in [18–20], the computationally excessive iteration procedure could be omitted using a relatively short (with regard to system's time constants) sample step and zero initial conditions for adjoint variables, yielding an optimal-based (suboptimal) control solution that is negligibly different from the optimal one. The control solution incorporates either two simultaneous control outputs: $u_1(t)$ (i.e., $i_{mr}(u, t)$) and $u_2(t)$ (i.e., $F_a(u, t)$) (H-MR-TVA system), or a single control output $u_1(t)$ (MR-TVA system).

The baseline weighting factors for the optimal-based control quality index (8) are assumed as follows: $g_{11} = 10^{21}$, $g_{12} = 10^{19}$, $g_{14} = 0$, $g_{21} = 4$, $g_{222} = 4 \times 10^{-12}$. The remaining weight values are given for each control case regarded below if they are nonzero (the omitted weights are assumed zero all over this section). A significant g_{12} value with regard to the previous research [21] is used to address transient states during simulated wave/wind realisations—incorporation of the protected structure velocity significant weight value corresponds to a derivative term of a displacement controller, which is known to be efficient during transients. A negligible but nonzero g_{222} value was selected to eliminate zero-division errors for $z_2(t) = z_4(t)$ in (23)–(25). The detailed weights of the quality function (8) were assumed as follows (*control cases I, II, III, I-H, II-H, III-H*):

- I** $g_{11} = 10^{21}$ and $g_{12} = 10^{19}$ —minimise the tower deflection and deflection rate as a sole objective (being the primary objective for all the control cases), MR-TVA used;
- II** $g_{13} = 3 \times 10^{19}$ (the TVA stroke weight) assumed in addition to *control case I* weights, MR-TVA used;
- III** $g_{15} = 10$ (the nacelle/tower tip acceleration weight) assumed in addition to *control case I* weights, MR-TVA used;
- I-H** as for *control case I*, H-MR-TVA used;
- II-H** as for *control case II*, H-MR-TVA used;
- III-H** as for *control case III*, H-MR-TVA used.

As a reference, an optimal-based, modified ground-hook law (*Mod.GH* using MR-TVA, and *Mod.GH-H* using H-MR-TVA) with the sole objective of the primary structure deflection minimisation is used [21], along with the passive TVA systems (*TVA-TN* and *TVA-TLP*).

7. Control Results

The efficiency of the considered solutions was analysed using the following quality indexes: tower tip relative displacement (i.e., tower deflection) root-mean-square (RMS) $rms(x_1 - x_0)$ (Figures 7 and 8), tower tip relative displacement (tower deflection) amplitude $A(x_1 - x_0)$ (Figures 9 and 10), TVA stroke amplitude $A(x_1 - x_2)$ (Figures 11 and 12), the MR damper force amplitude (Figures 13 and 14; *Mod.GH* and *Mod.GH-H* results excluded due to seriously outlying values—see Table 5), and mean actuator power (Figure 15), along with the time patterns of x_0 , x_1 , $x_1 - x_2$, F_a , and F_{mr} (Figures 16–18) and Table 5 ($A(\bullet)$ states for the amplitude, i.e., the maximum deviation from the equilibrium state). The $rms(x_1 - x_0)$ (equal to the standard deviation for zero mean value) value indicates the tower structure operational fatigue, the tower deflection amplitude $A(x_1 - x_0)$ indicates the maximum structural stress, whereas the TVA stroke amplitude $A(x_1 - x_2)$ determines the spatial and structural applicability of the vibration control solution; the required MR damper force F_{mr} , associated with the particular solution, conditions its efficiency. In Table 5, the most favourable results are marked in green boldface, the worst results are marked in red boldface, whereas the runner-up solutions are marked in green/red (respectively) regular face.

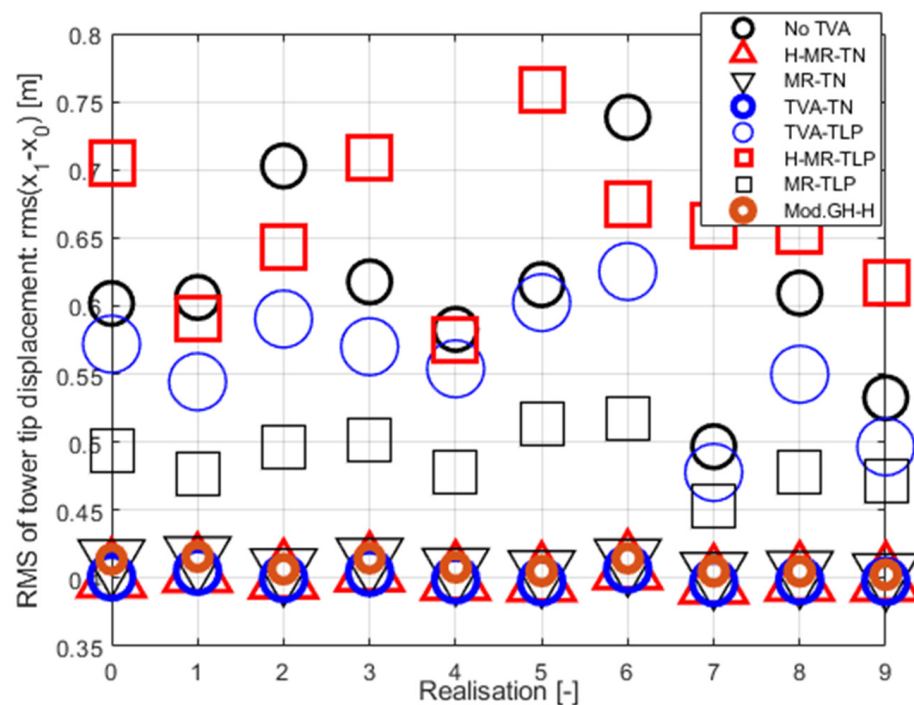


Figure 7. RMS of tower tip relative displacement $rms(x_1 - x_0)$ for $g_{11} = 10^{21}$ and $g_{12} = 10^{19}$. Results summary.

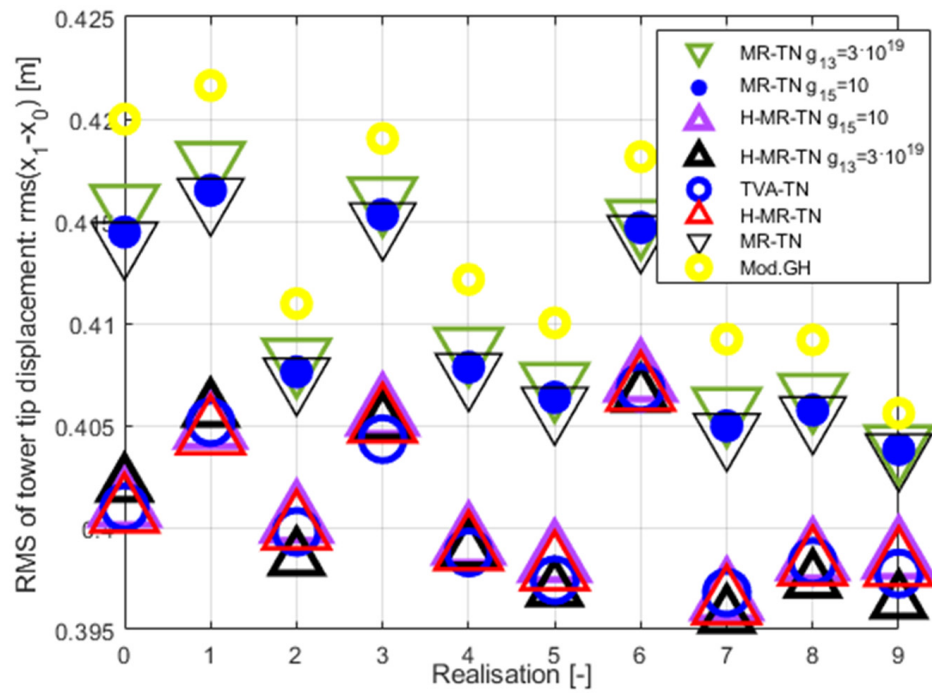


Figure 8. RMS of tower tip relative displacement $rms(x_1 - x_0)$ for $g_{11} = 10^{21}$ and $g_{12} = 10^{19}$. TVA tuned to the NREL 5MW tower-nacelle 1st bending mode.

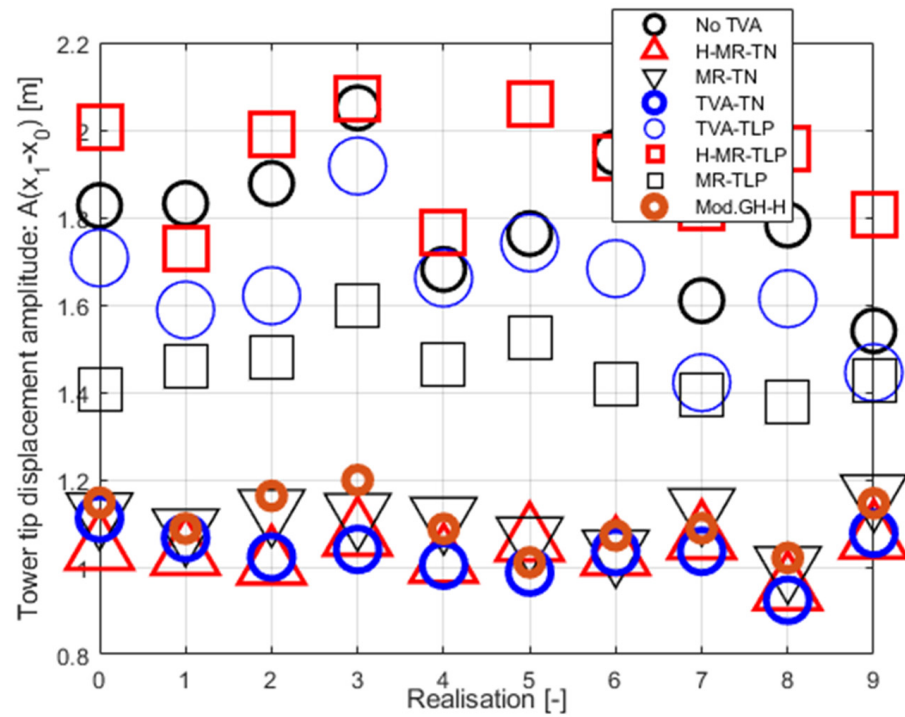


Figure 9. Tower tip relative displacement amplitude $A(x_1 - x_0)$ for $g_{11} = 10^{21}$ and $g_{12} = 10^{19}$. Results summary.

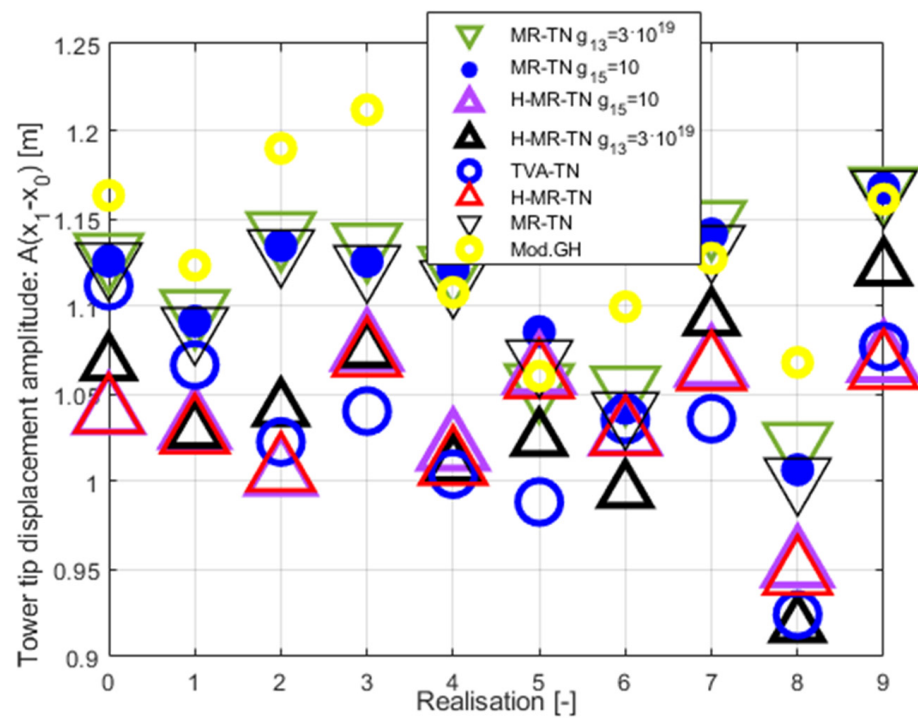


Figure 10. Tower tip relative displacement amplitude $A(x_1 - x_0)$ for $g_{11} = 10^{21}$ and $g_{12} = 10^{19}$. TVA tuned to the NREL 5MW tower-nacelle 1st bending mode.

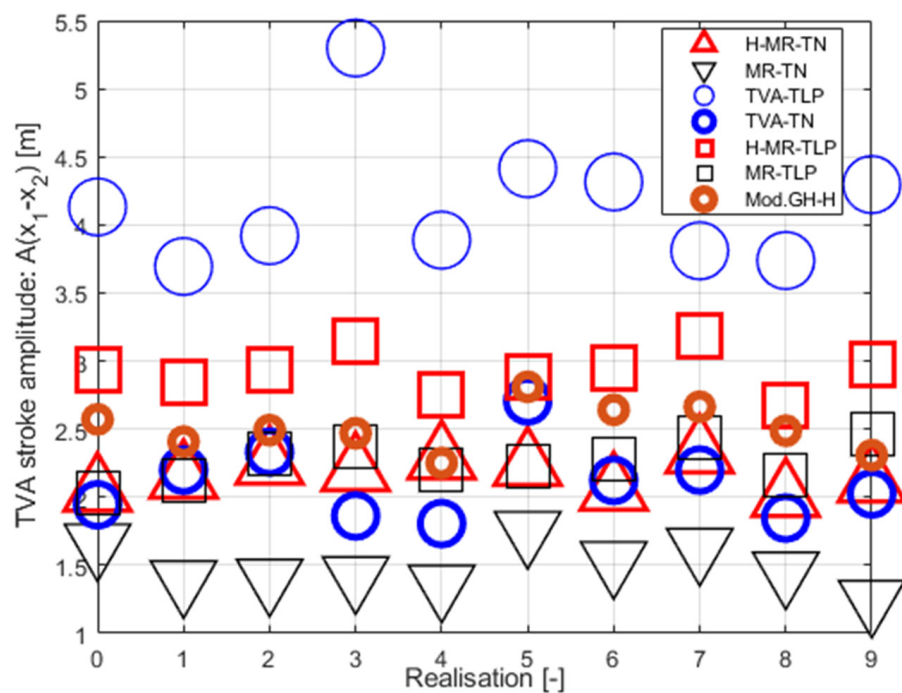


Figure 11. TVA stroke amplitude $A(x_1 - x_2)$ for $g_{11} = 10^{21}$ and $g_{12} = 10^{19}$. Results summary.

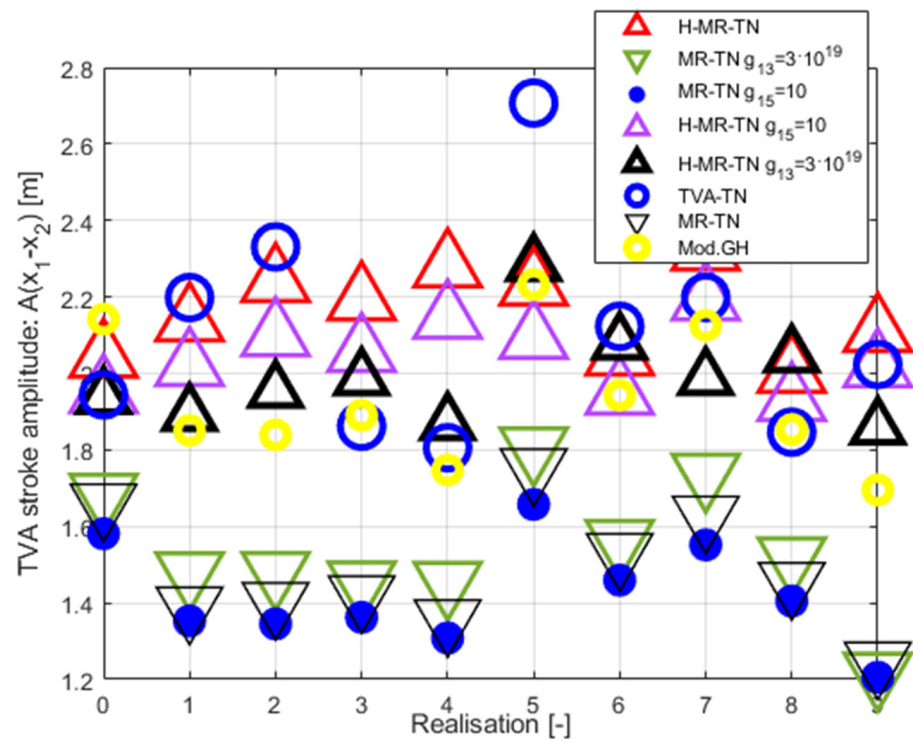


Figure 12. TVA stroke amplitude $A(x_1 - x_2)$ for $g_{11} = 10^{21}$ and $g_{12} = 10^{19}$. TVA tuned to the NREL 5MW tower-nacelle 1st bending mode.

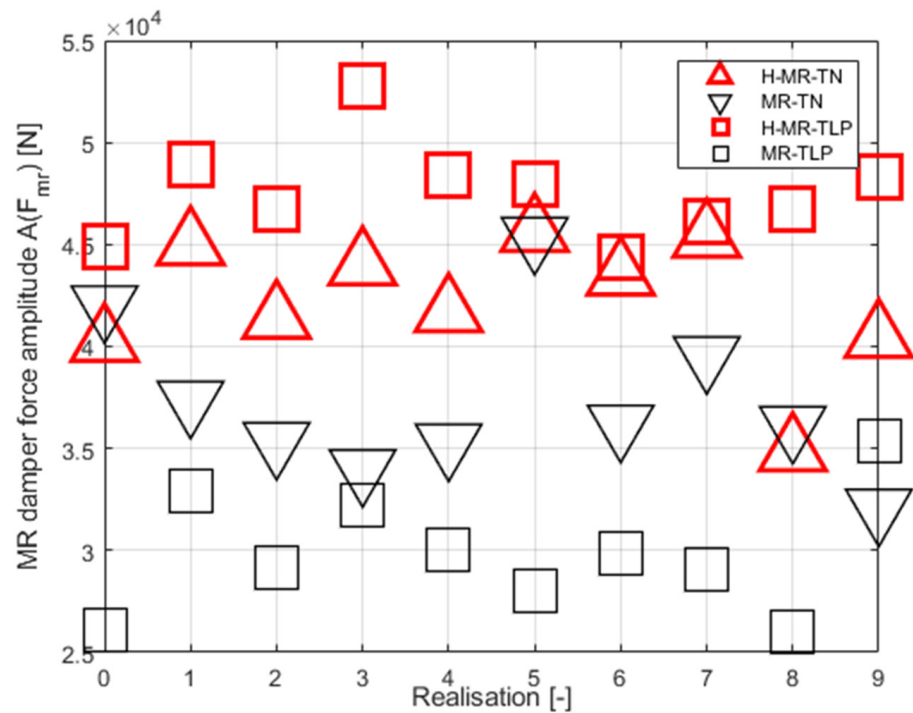


Figure 13. MR damper force amplitude $A(F_{mr})$ for $g_{11} = 10^{21}$ and $g_{12} = 10^{19}$. Results summary.

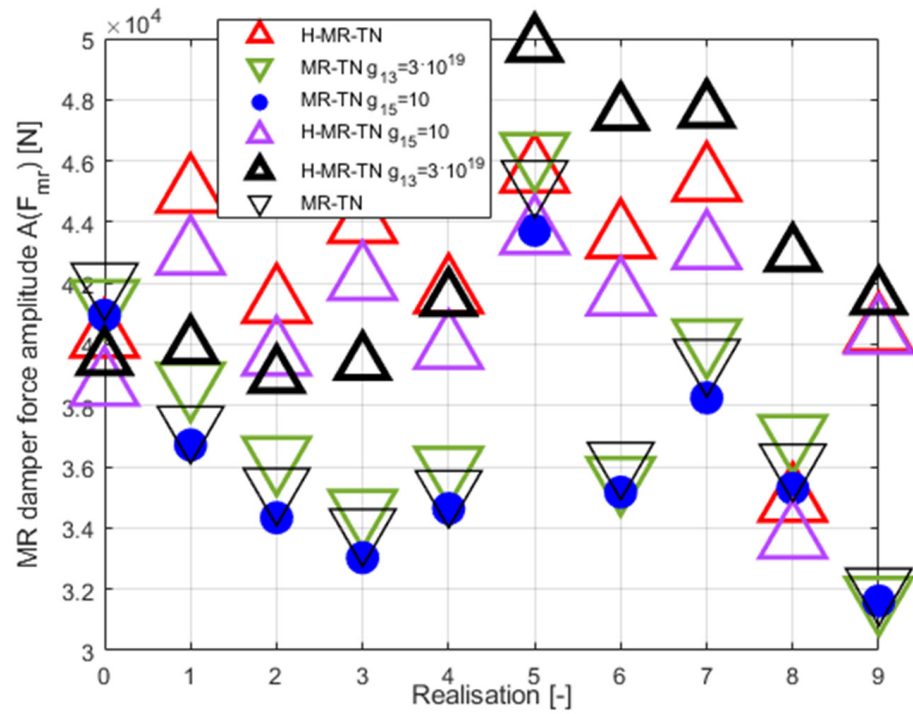


Figure 14. MR damper force amplitude $A(F_{mr})$ for $g_{11} = 10^{21}$ and $g_{12} = 10^{19}$. TVA tuned to the NREL 5MW tower-nacelle 1st bending mode.

Table 5. The test cases' cumulative results over realisations 0 ÷ 9 (baseline weights: $g_{11} = 10^{21}$, $g_{12} = 10^{19}$, $g_{14} = 0$, $g_{21} = 4$, $g_{222} = 4 \times 10^{-12}$ assumed for control cases I, II, III, I-H, II-H, III-H).

Index	Test Cases	No TVA	Passive TVA	Mod. GH	Control	Control	Control	Mod. GH-H	Control	Control	Control
					Case I $g_{13} = 0$ $g_{15} = 0$	Case II $g_{13} = 3 \cdot 10^{19}$ $g_{15} = 0$	Case III $g_{13} = 0$ $g_{15} = 10$		Case I-H $g_{13} = 0$ $g_{15} = 0$	Case II-H $g_{13} = 3 \cdot 10^{19}$ $g_{15} = 0$	Case III-H $g_{13} = 0$ $g_{15} = 10$
TVA-TN	$\sum_{0.9} rms(x_1 - x_0)$	6.104	4.006	4.136	4.094	4.105	4.097	4.092	4.006	4.003	4.010
	10	$\cdot 10^{-1}$	$\cdot 10^{-1}$	$\cdot 10^{-1}$	$\cdot 10^{-1}$	$\cdot 10^{-1}$	$\cdot 10^{-1}$	$\cdot 10^{-1}$	$\cdot 10^{-1}$	$\cdot 10^{-1}$	$\cdot 10^{-1}$
	$\max_{0.9} A(x_1 - x_0)$	2.050	1.112	1.212	1.166	1.168	1.168	1.199	1.072	1.121	1.075
	$\max_{0.9} A(x_1 - x_2)$			2.707	2.232	1.752	1.806	1.658	2.810	2.322	2.284
	$\max_{0.9} A(F_{mr})$			57.46	45.38	46.25	43.73	69.13	45.62	49.78	43.61
TVA-TLP	$\sum_{0.9} rms(x_1 - x_0)$	6.104	5.582		4.880				6.589		
	10	$\cdot 10^{-1}$	$\cdot 10^{-1}$		$\cdot 10^{-1}$				$\cdot 10^{-1}$		
	$\max_{0.9} A(x_1 - x_0)$	2.050	1.917		1.599				2.070		
	$\max_{0.9} A(x_1 - x_2)$			5.299	2.458				3.185		
	$\max_{0.9} A(F_{mr})$				35.32				52.75		

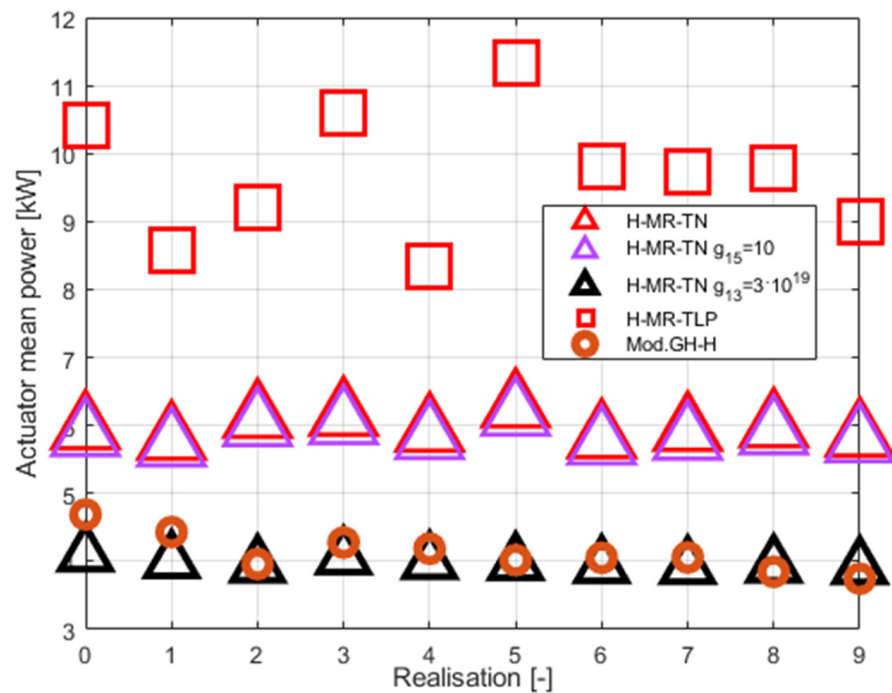


Figure 15. Mean actuator power P_a .

Figures 7 and 8 present tower tip relative displacement RMS values obtained for the $0 \div 9$ Bredsneder spectrum ocean wave realisations paired with Weibull distribution wind patterns. The TVA was tuned either to the NREL 5MW tower-nacelle first bending mode case (*H-MR-TN* legend for *H-MR-TVA* case; *MR-TN* legend for *MR-TVA* case), or to the TLP surge frequency case (*H-MR-TLP* legend for *H-MR-TVA* case; *MR-TLP* legend for *MR-TVA* case). Figures 9 and 10 present tower tip relative displacement amplitudes for the same set of ten ocean wave/wind realisations for the TVA tuned to the tower-nacelle first bending mode or the TLP surge frequency. Similarly, Figures 11 and 12/Figures 13 and 14 present the TVA stroke amplitudes/MR damper force amplitudes (respectively), whereas Figure 15 presents the mean actuator power values obtained for *TVA-TN* cases. The regarded control solutions comparison, covering the vibration attenuation results cumulated over all $0 \div 9$ wave/wind realisations, is presented in Table 5, including the mean of RMSs of tower tip relative displacements (tower deflections) $\frac{1}{10} \sum_{0:9} rms(x_1 - x_0)$, tower tip relative displacements (tower deflections) maximum amplitudes $\max_{0:9} A(x_1 - x_0)$, TVA stroke maximum amplitudes $\max_{0:9} A(x_1 - x_2)$, and MR damper force maximum amplitudes $\max_{0:9} A(F_{mr})$.

Based on the obtained results, the general conclusion regarding the TVA tuning frequency is consistent with the previous work [33], i.e., the *TVA-TN* solution is by far superior to the *TVA-TLP* one regarding tower deflection RMS/amplitude and TVA stroke values. Thus, only the *TVA-TN* case was selected for the more thorough analyses described below. The obtained values of the maximum tower tip relative displacement (tower deflection) amplitude $A(x_1 - x_0)$ indicate that under the assumed extreme wave/wind conditions, the regarded TLP–NREL 5MW structures without a TVA (or any other vibration attenuation solution) or with a TVA tuned to the TLP surge frequency (especially passive and hybrid *TVA-TLPs*) are at risk of tower structural failure, which starts to occur when the tower deflection reaches 2.2 m according to the research [31]. All the regarded *TVA-TN* solutions provide a tower structural deflection safety factor of ca. 2 following [31], which is a quite conservative estimate as the TLP surge motion is assumed uninfluenced by the wind turbine tower bending; in fact, tower-reaction-driven TLP motion contributes to lowering the tower deflection.

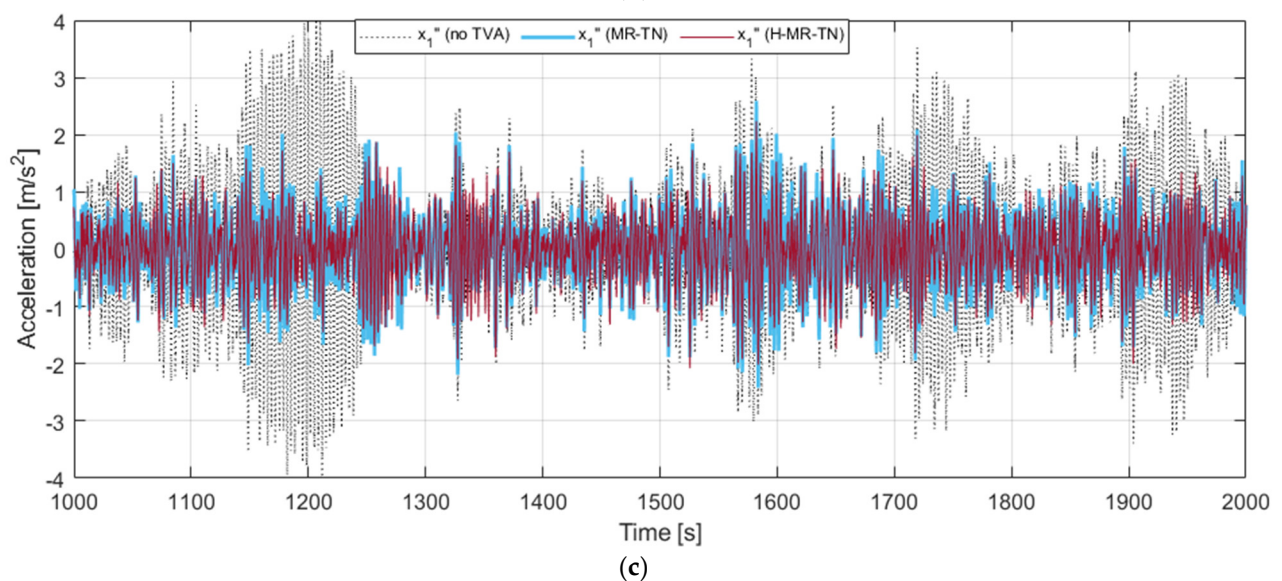
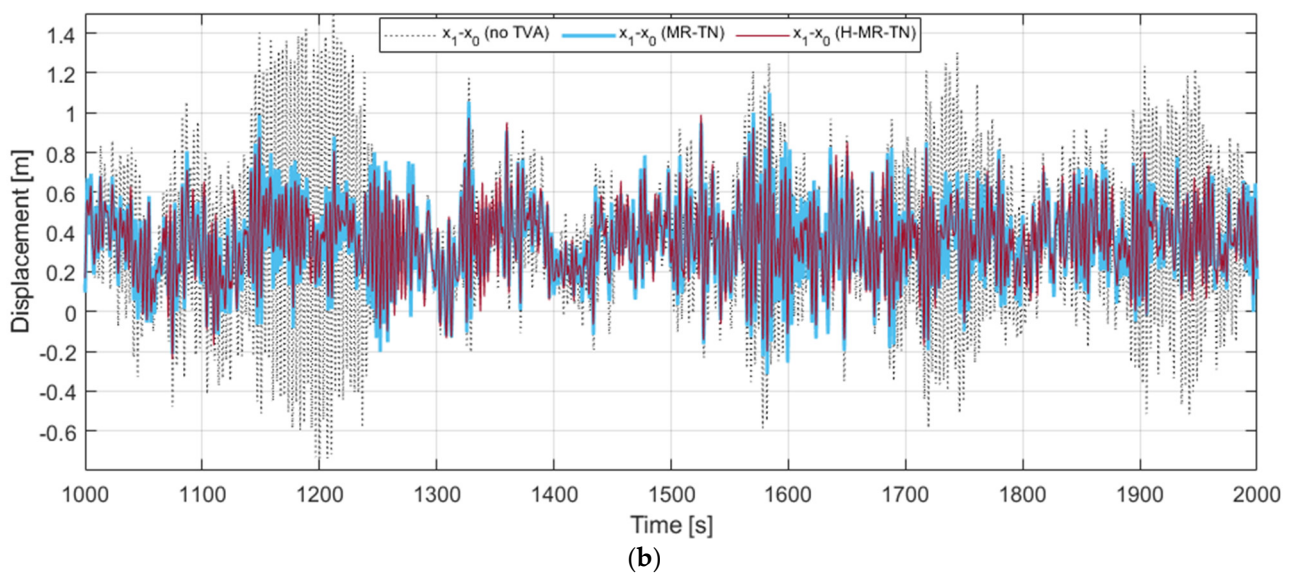
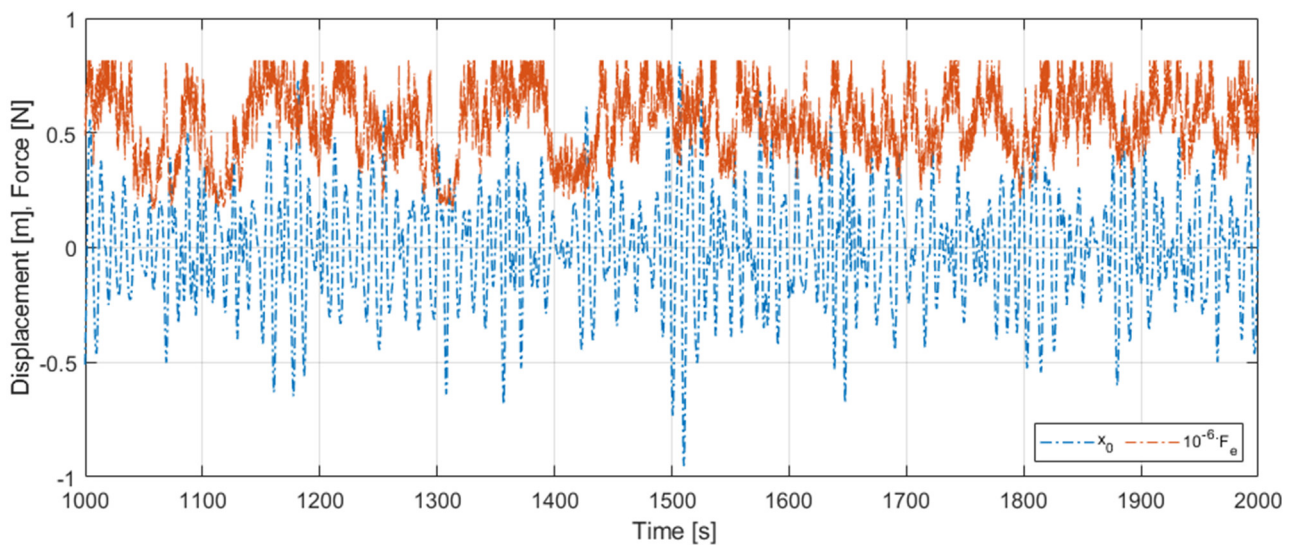


Figure 16. Time patterns for exemplary *Realisation 7*: (a) TLP surge x_0 combined with the nacelle horizontal load F_e , (b) tower tip relative displacement (tower deflection), (c) nacelle acceleration.

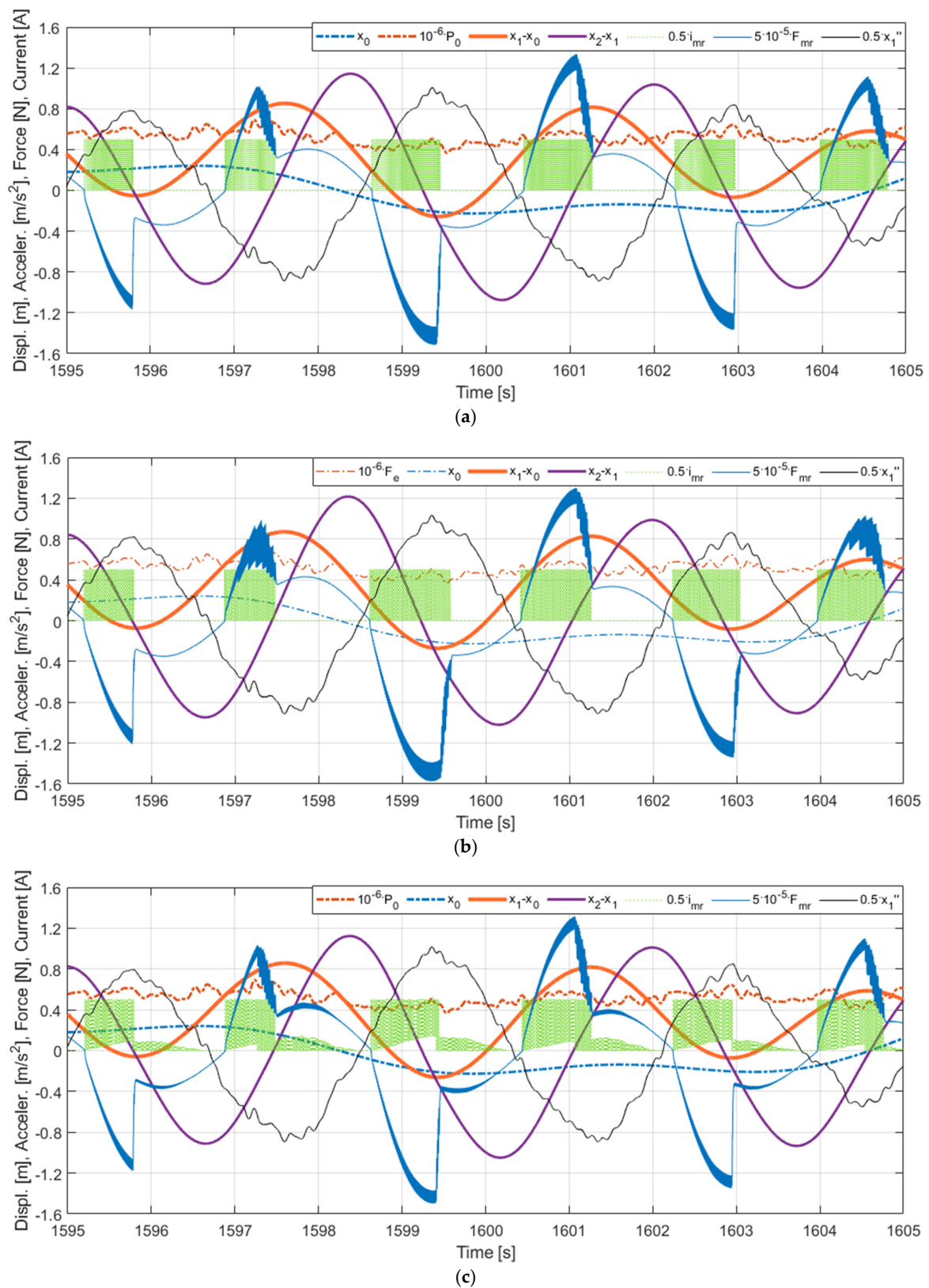


Figure 17. Time responses for MR-TVA tuned to the NREL 5MW tower-nacelle 1st bending mode: (a) Control case I, (b) Control case II, (c) Control case III (Realisation 7).

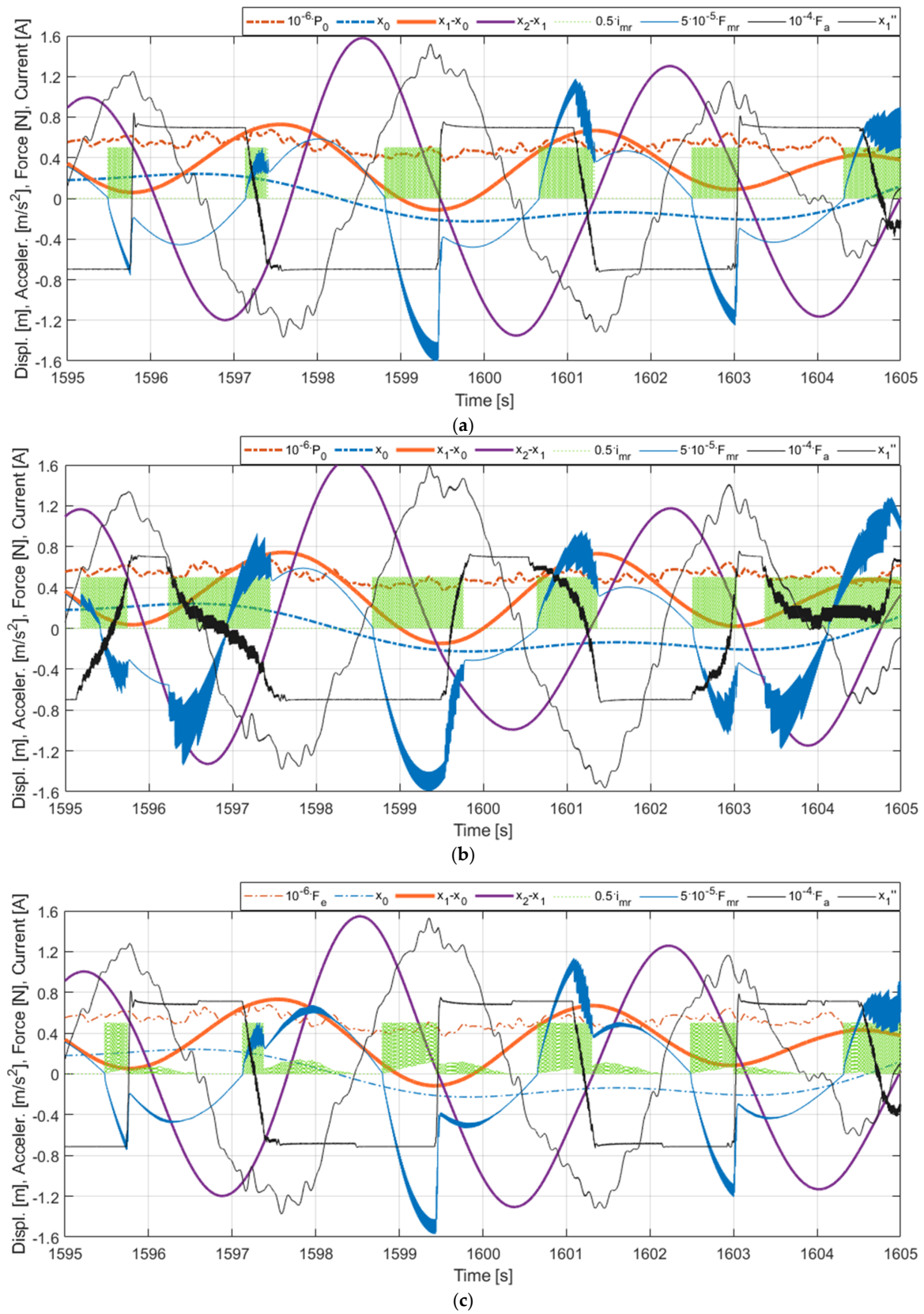


Figure 18. Time responses for H-MR-TVA tuned to the NREL 5MW tower-nacelle 1st bending mode: (a) Control case I-H, (b) Control case II-H, (c) Control case III-H (Realisation 7).

The results shown in Figures 7–10 and Table 5 indicate mixed benefits of the force actuator utilisation in the TVA system. Up to a 2.5% cumulative (i.e., across all ten ocean

wave/wind realisations, see Table 5) minimisation in the RMS tower deflection, along with up to an 8.8% tower deflection amplitude minimisation in the *TVA-TN* case, at the cost of up to 32.5% increased TVA stroke, is the result of the implementation of this active machinery along with the control circuitry and computation resources for the H-MR-TVA system vs. the MR-TVA one (BTW, a significant increase in the tower deflection RMSs/amplitudes, TVA strokes, and MR damper force amplitudes may be observed for the active actuator utilisation in the *TVA-TLP* case). The MR damper is a semi-active, dissipative device, which force F_{mr} attenuates the relative travel of the protected structure and the absorber. In contrast, the active actuator repetitively generates the force F_a of the opposite sign, leading to the primary structure deflection and acceleration minimisation through the TVA stroke extension (see Figure 18 vs. Figure 17), as observed for all the regarded H-MR-TVA systems vs. MR-TVA systems (Table 5).

According to the definition of the amplitude, $A(\bullet)$, the TVA effective peak-peak travel distance has to be regarded as $2A(x_1 - x_2)$, i.e., twice the value from Table 5 and Figures 11 and 12. Thus, passive TVA solutions with 10-ton absorber mass (including the *TVA-TN* solution with 5.414 m TVA total travel distance) as well as the *Mod.GH-H* solution cannot be implemented along the demanding side-side direction in the nacelle without enforcing end-stop collision bumpers, which limit the TVA stroke but result in efficiency deterioration concerning the results presented in Table 5 and Figures 7–10. Therefore, the promising tower deflection indexes of the passive *TVA-TN* system are hardly realisable, considering the NREL 5MW nacelle dimensions (Table 1) [28]. The H-MR-TVA travel distance values' admissibility must be confirmed before implementation. However, *control case III-H* may be regarded as applicable with proper g_{15} weight selection (i.e., a possible increase concerning $g_{15} = 10$ assumed here).

The superiority of the newly developed optimal-based solutions (*control case I(-H)*, *II(-H)*, *III(-H)*) over the baseline *Mod.GH(-H)* control law is evident, especially regarding maximum tower deflection amplitude (up to 10.3% reduction) and TVA stroke amplitude (up to 25.7% reduction) values, and the MR damper force amplitudes to even further extend (up to 36.9% reduction). The modified ground-hook approach is devoted to the case when only the protected structure's relative displacement (tower deflection) has to be minimised. In contrast, the redeveloped *control case I(-H)*, *II(-H)*, and *III(-H)* uses various optimisation fields (i.e., the nacelle relative velocity and acceleration, or the TVA stroke length) embedded in quality function (8), and the MR damper/force actuator constraints embedded in state and co-state Equations (4) and (11), to produce more favourable results.

Figures 16–18 present selected time characteristics obtained for the exemplary wave/wind realisation no. 7: the excitations (TLP surge x_0 combined with the nacelle horizontal load F_e), the relative displacements of the tower tip (tower deflection $x_1 - x_0$) and the TVA ($x_2 - x_1$), the nacelle acceleration \ddot{x}_1 , the force produced by the MR damper F_{mr} (and the electromagnetic actuator F_a for the H-MR-TVA system only), and the MR damper electric current i_{mr} , obtained for the TVA tuned to the NREL 5MW tower-nacelle 1st bending mode vs. the structure without the TVA (tower deflection for the latter only; mind the signals multipliers in the legends). Figure 16a–c present the excitations' time patterns and the corresponding tower tip relative displacement and nacelle acceleration responses obtained for the system without the TVA and two (H-)MR-TVA solutions: *MR-TN (control case I)* and *H-MR-TN (control case I-H)*. Figure 17a vs. Figure 17b vs. Figure 17c show comparable time histories, zoomed in along the time axis to illustrate the control action for the MR-TVA system, while Figure 18a vs. Figure 18b vs. Figure 18c—for the H-MR-TVA system. As is evident in Figure 16, both MR-TVA and H-MR-TVA substantially reduce tower deflection and nacelle acceleration amplitudes, although the additional force actuator operation of the latter yields preferable protected structure vibration mitigation results. The operation of the MR-TVA system (Figure 17), *control case II* vs. *control case I*, is characterised by the slightly increased MR damper force modulus mostly during time intervals of high absorber velocity (both $\dot{x}_2 - \dot{x}_1$ and $\dot{x}_2 - \dot{x}_0$) values and the appropriate F_{mr} sign, opposing the absorber's drawing away from the primary structure. On the other hand, the operation of

the *control case III* solution vs. *control case I* and *control case II* is indicated with nonzero MR damper current during time intervals when force F_{mr} opposes the maximum acceleration \ddot{x}_1 values. The optimal control task quality function (8) is aimed to minimise the H_2 norm of the included quantities; thus, the maximum amplitude of the TVA stroke is, in fact, not reduced for *control case II* solution vs. *control case I* (Figure 12 and Table 5), as for *control case III*. However, the TVA stroke RMS value is actually slightly lower for *control case II* vs. *control case I* and *control case III* (0.346 m vs. 0.353 m and 0.348 m, respectively, for the regarded exemplary *Realisation 7* response, see Figure 17). The operation of the H-MR-TVA system (Figure 18), *control case II-H* and *control case III-H* vs. *control case I-H*, exhibits similar MR damper control i_{mr} conditions as described for the MR-TVA system. However, TVA stroke amplitude and RMS values are both reduced for *control case II-H* and *control case III-H* with regard to *control case I-H*, thanks to the active force actuator support. When analysing Figure 18a–c, it is evident that both actuators' forces are used in cooperation by the vibration control system, e.g., in Figure 18c, the F_{mr} modulus increased due to the increased (concerning Figure 18a,b) MR damper current i_{mr} is reflected by the decreased F_a modulus. Moreover, most F_a transients are accompanied by the F_{mr} support, as the MR damper response (27) is faster than the assumed electromagnetic force actuator's (28). The MR damper force F_{mr} support for the *control case II-H* solution, as visible in Figure 18b, also leads to the mean actuator power reduction (see Figure 15, H-MR-TN $g_{13} = 3 \times 10^{19}$ legend).

Implementing the protected structure's acceleration term $g_{15}\dot{z}_2^2(t)$ in the quality index (8) reduces the TVA stroke amplitude $A(x_1 - x_2)$ more effectively than using the $g_{13}(z_1(t) - z_3(t))^2$ term and, apart from that, the required MR damper force amplitude is also reduced, as reflected in Figures 12, 14, 17 and 18 and Table 5. It also is worth to mention that the $g_{13}(z_1(t) - z_3(t))^2$ term used here for the MR-TVA system (*control case II*) is ineffective in $A(x_1 - x_2)$ minimisation (see Figures 12 and 17b and Table 5); at the same time, it marginally deteriorates the primary structure response (Figures 8, 10 and 17a,b and Table 5). For the H-MR-TVA, *control case II-H* yields both less favourable primary structure deflection and less favourable TVA stroke length than *control case III-H*, i.e., similar mean tower deflection RMS values but 4.3% higher maximum tower deflection amplitude, and 4.3% higher maximum TVA stroke amplitude over all wave/wind realisations (see Table 5). On the contrary, the $g_{15}\dot{z}_2^2(t)$ term implementation for the MR-TVA (*control case III*) results in 9.0% and 5.7% maximum TVA stroke amplitude reduction over all wave/wind realisations with regard to *control case II* and *control case I*, respectively, while its primary structure response differences with regard to the preferable *control case I* (Figures 8, 10 and 17 and Table 5) are negligible (within 0.2%). The implementation of the $g_{15}\dot{z}_2^2(t)$ term for the H-MR-TVA system (*control case III-H*) results in 6.0% maximum TVA stroke amplitude reduction concerning the baseline *control case I-H*, while the primary structure response differences are negligible (within 0.3%), as for the MR-TVA system. The TVA travel distance reductions are obtained thanks to the sole control algorithm alteration. Thus, no additional hardware/software resources are necessary, while this pure advantage is accompanied by up to 4.4% reduction in the MR damper force amplitude vs. the *control case I(-H)* solutions.

Concerning the limited TVA stroke, the most favourable vibration control solution is the semi-active MR-TVA *control case III* implementation, providing favourable cumulative primary structure deflection indexes (over all wave/wind realisations) at the lowest obtained TVA travel distance. A possible alternative is the hybrid H-MR-TVA *control case III-H* implementation, providing even more favourable cumulative primary structure deflection indexes and reduced nacelle acceleration levels thanks to the utilisation of the force actuator of relatively low mean power (up to 6.15 kW), of which one side effect is, however, the increased TVA travel distance.

8. Conclusions

The purpose of this research was the implementation and numerical study of the nonlinear optimal-based vibration control solutions for the full-scale TLP–NREL 5MW

wind turbine tower-nacelle model with the (H-)MR-TVA vibration reduction system under excessive wave/wind polyperiodic excitations yielding continual transient vibration states. The selection of the tuning frequency was initially investigated, and the TVAs were tuned to the tower-nacelle 1st bending mode (*TVA-TN*) or the TLP surge frequency (*TVA-TLP*). Simulations using experimentally derived platform motion realisations were performed, and the two approaches were compared based on tower deflection amplitude/RMS and TVA stroke values. It was concluded that the *TVA-TN* approach is superior to the *TVA-TLP* one. All the considered *TVA-TN* solutions provide a tower deflection safety factor of ca. 2, while the structure without any vibration reduction solutions or with the TVA tuned to the TLP surge frequency (especially passive and hybrid *TVA-TLPs*) are at risk of tower structural failure.

TVAs utilising magnetorheological dampers (MR-TVAs) either without or with additional small-scale active actuators (forming hybrid H-MR-TVAs) were examined, considering three control strategies for each TVA type. The *control case I/I-H* includes weighting factors for the minimisation of tower deflection and deflection rate. The *control case II/II-H* additionally assumes the nonzero weighting factor for the TVA stroke; in contrast, the *control case III/III-H* adds the nonzero weighting factor for the nacelle (tower tip) acceleration. The performance of these solutions was compared against the well-proven baseline modified ground-hook law (*Mod.GH/Mod.GH-H*), which uses the minimisation of the primary structure deflection as the single objective in the control strategy. The comparisons revealed that the newly proposed implementation of the protected structure's acceleration and nonzero relative velocity terms (*control case III/III-H*) in the quality function results in 25.7%/22.0% maximum TVA stroke amplitude reduction along with 3.6%/10.3% maximum tower deflection amplitude reduction for the MR-TVA/H-MR-TVA systems, respectively. Furthermore, the sole usage of the protected structure's acceleration term yields ca. 6% maximum TVA stroke amplitude reduction with regard to the *control case I* and *I-H* approaches, while the tower deflection response differences are negligible. The TVA travel distance reductions are obtained thanks to the sole control algorithm enhancement. Thus, no additional resources are necessary, while reducing the MR damper force necessary for the TVA operation accompanies this pure advantage. The utilisation of the protected structure's acceleration term reduces the TVA stroke amplitude more efficiently than standard TVA relative displacement term usage, as in the previously developed approach (the latter being ineffective for the MR-TVA implementation), which, in turn, efficiently reduces the TVA stroke RMS (H_2 norm) values and, apart from that, the required mean actuator power for the H-MR-TVA implementation.

Regarding the limited TVA stroke, the most favourable solution is the semi-active *control case III*, guarantying favourable cumulative primary structure deflection indexes at the lowest obtained TVA travel distance. A possible alternative may be the hybrid *control case III-H*, providing even more favourable primary structure deflection qualities (8% lower deflection amplitude) and reduced nacelle acceleration levels thanks to the utilisation of the force actuator of the relatively low power (ca. 6 kW). However, this has the side effect of an increased TVA stroke amplitude. The analysed passive TVA systems (both *TVA-TN* and *TVA-TLP*) with a relatively small 10-ton absorber mass can hardly be implemented in the nacelle, especially along the demanding side-side direction, without enforcing end-stop collision bumpers, which result in efficiency deterioration.

The results of the current study may be used in the design process of the full-scale vibration reduction system attached to the real-world NREL 5MW-class floating, TLP-based wind turbine structure. No offline calculations, MR damper or actuator (servomotor) force tracking, disturbances, or dominant frequency assumption are necessary for proper real-time implementation of the proposed method. This implementation includes complex polyperiodic vibration states arising from the variable waves and wind excitations. However, the developed approach may be directly applied to transient and steady-state structural vibration control under various other stochastic and deterministic disturbances. This crucial problem will be further investigated considering the FOWT model extension utilis-

ing a dedicated finite element environment in combination with the MATLAB/Simulink simulation platform.

Author Contributions: Conceptualization, P.M.; Methodology, P.M.; Software, P.M. and G.M.K.; Validation, P.M., G.M.K. and S.A.M.; Formal analysis, P.M.; Investigation, P.M.; Resources, P.M., G.M.K. and S.A.M.; Data curation, P.M.; Writing—original draft, P.M.; Writing—review & editing, P.M. and G.M.K.; Visualization, P.M. and G.M.K.; Supervision, P.M.; Project administration, P.M.; Funding acquisition, P.M. All authors have read and agreed to the published version of the manuscript.

Funding: The research project was supported by the program “Excellence initiative—research university” for the AGH University.

Data Availability Statement: The data presented in this study are available on request.

Conflicts of Interest: The authors declare no conflict of interest.

List of Symbols Used:

<i>Symbol</i>	<i>Value</i>	<i>Unit</i>	<i>Description</i>
m_1	428.8×10^3	kg	modal mass of the NREL 5MW tower 1st bending mode
m_2	10.0×10^3	kg	mass of the absorber
k_1	1.546×10^6	N/m	modal stiffness of the NREL 5MW tower 1st bending mode
k_2	34.42×10^3	N/m	stiffness coefficient of the absorber tuned to the NREL 5MW tower 1st bending mode
	3.770×10^3	N/m	stiffness coefficient of the absorber tuned to the TLP surge
c_1	3.542×10^3	Ns/m	modal damping of the NREL 5MW tower 1st bending mode
c_2	3.352×10^3	Ns/m	damping coefficient of the passive absorber tuned to the NREL 5MW tower 1st bending mode
	1.109×10^3	Ns/m	damping coefficient of the passive absorber tuned to the TLP surge
i_{max}	1.0	A	maximum current of the magnetorheological damper
C_1	1581	N/A	current-dependent friction coefficient
C_2	38.25	N	friction coefficient
		Ns/Am	current-dependent
C_3	12,240	viscous damping coefficient	viscous damping coefficient
C_4	3570	Ns/m	viscous damping coefficient
ν	1300	s/m	friction scaling parameter
p	1	1/s	hysteresis scaling parameter
F_{nom}	7125	N	nominal force of the actuator
g_{11}	10^{21}	$1/m^2$	weight of the protected structure relative displacement
g_{12}	10^{19}	s^2/m^2	weight of the protected structure relative velocity
g_{13}	3×10^{19}	$1/m^2$	weight of the absorber relative displacement
g_{14}	0	s^2/m^2	weight of the absorber relative velocity
g_{15}	10	s^4/m^2	weight of the protected structure acceleration
g_{21}	4	$1/A^2$	weight of the magnetorheological damper current
g_{221}	0	$1/N^2$	weight of the magnetorheological damper force
g_{222}	4×10^{-12}	$1/N^2$	weight of the actuator force

g_{23}	0	$1/W^2$	weight of the actuator power
F_{mr}		N	force generated by the magnetorheological damper
F_a		N	force generated by the actuator
P_a		N	power of the actuator
F_e		N	rotor force excitation
x_0		m	TLP surge excitation
z_1, x_1		m	horizontal displacement of the nacelle
z_2, \dot{x}_1		m/s	horizontal velocity of the nacelle
z_3, x_2		m	horizontal displacement of the absorber
z_4, \dot{x}_2		m/s	horizontal velocity of the absorber

References

- Weber, F.; Maślanka, M. Precise stiffness and damping emulation with MR dampers and its application to semi-active tuned mass dampers of Wolgograd Bridge. *Smart Mater. Struct.* **2014**, *23*, 15019. [\[CrossRef\]](#)
- Kavyashree, B.G.; Patil, S.; Rao, V.S. Review on vibration control in tall buildings: From the perspective of devices and applications. *Int. J. Dyn. Control* **2020**, *9*, 1316–1331. [\[CrossRef\]](#)
- Caterino, N. Semi-active control of a wind turbine via magnetorheological dampers. *J. Sound Vib.* **2015**, *345*, 1–17. [\[CrossRef\]](#)
- Kirkegaard, P.H.; Nielsen, S.R.K.; Poulsen, B.L.; Andersen, J.; Pedersen, L.H.; Pedersen, B.J. Semiactive vibration control of a wind turbine tower using an MR damper. In *Structural Dynamics—EURODYN*; Grundmann, H., Schueller, G.I., Eds.; Swets & Zeitlinger: Lisse, The Netherlands, 2002.
- Yung-Yen, K. A simplified structural model for monopile-supported offshore wind turbines with tapered towers. *Renew. Energy* **2020**, *156*, 777–790.
- Alotta, G.; Biondo, C.; Giaralis, A.; Failla, G. Seismic protection of land-based wind turbine towers using the tuned inerter damper. *Structures* **2023**, *51*, 640–656. [\[CrossRef\]](#)
- Rotea, M.A.; Lackner, M.A.; Saheba, R. Active Structural Control of Offshore Wind turbines. In Proceedings of the 48th AIAA Aerospace Sciences Meeting Including the New Horizons Forum and Aerospace Exposition, Orlando, FL, USA, 4–7 January 2010.
- Tsouroukdissian, A.; Carcangiu, C.E.; Pineda, A.I.; Martin, M.; Fischer, T.; Kuhnle, B.; Scheu, M. Wind Turbine Tower Load Reduction using Passive and Semiactive Dampers. In Proceedings of the European Wind Energy Association Annual Event, Brussels, Belgium, 14–17 March 2011.
- Spencer, B.F., Jr.; Soong, T.T. New Applications and Development of Active, Semi-Active and Hybrid Control Techniques for Seismic and Non-Seismic Vibration in the USA. In Proceedings of the International Post-SMiRT Conference Seminar on Seismic Isolation, Passive Energy Dissipation and Active Control of Vibration of Structures, Cheju, Republic of Korea, 23–25 August 1999.
- Zhang, Z.; Staino, A.; Basu, B.; Nielsen, S.R.K. Performance evaluation of full-scale tuned liquid dampers (TLDs) for vibration control of large wind turbines using real-time hybrid testing. *Eng. Struct.* **2016**, *126*, 417–431. [\[CrossRef\]](#)
- Den Hartog, J.P. *Mechanical Vibrations*; Dover Publications: Mineola, NY, USA, 1985.
- Nakamura, Y.; Tanaka, K.; Nakayama, M.; Fujita, T. Hybrid mass dampers using two types of electric servomotors: AC servomotors and linear-induction servomotors. *Earthq. Eng. Struct. Dyn.* **2001**, *30*, 1719–1743. [\[CrossRef\]](#)
- Preumont, A.; Alaluf, D.; Bastait, R. Hybrid Mass Damper: A Tutorial Example. In *Active and Passive Vibration Control of Structures*; Hagedorn, P., Spelsberg-Korspeter, G., Eds.; CISM International Centre for Mechanical Sciences: Udine, Italy, 2014. [\[CrossRef\]](#)
- Demetriou, D.; Nikitas, N. A Novel Hybrid Semi-Active Mass Damper Configuration for Structural Applications. *Appl. Sci.* **2016**, *6*, 397. [\[CrossRef\]](#)
- Koo, J.H.; Ahmadian, M. Qualitative Analysis of Magneto-Rheological Tuned Vibration Absorbers: Experimental Approach. *J. Intell. Mater. Syst. Struct.* **2007**, *18*, 1137–1142. [\[CrossRef\]](#)
- Wang, L.; Liang, Z.; Cai, M.; Zhang, Y.; Yan, J. Adaptive Structural Control of Floating Wind Turbine with Application of MR Damper. *Energy Procedia* **2019**, *158*, 254–259. [\[CrossRef\]](#)
- Martynowicz, P. Control of an MR Tuned Vibration Absorber for Wind Turbine Application Utilising the Refined Force Tracking Algorithm. *J. Low Freq. Noise Vib. Act. Control* **2017**, *36*, 339–353. [\[CrossRef\]](#)
- Martynowicz, P. Nonlinear optimal-based vibration control for systems with MR tuned vibration absorbers. *J. Low Freq. Noise Vib. Act. Control* **2019**, *38*, 1607–1628. [\[CrossRef\]](#)
- Martynowicz, P. Real-time implementation of nonlinear optimal-based vibration control for a wind turbine model. *J. Low Freq. Noise Vib. Act. Control* **2019**, *38*, 1635–1650. [\[CrossRef\]](#)
- Martynowicz, P. Nonlinear Optimal-Based Vibration Control of a Wind Turbine Tower Using Hybrid vs. Magnetorheological Tuned Vibration Absorber. *Energies* **2021**, *14*, 5145. [\[CrossRef\]](#)
- Martynowicz, P. Experimental study on the optimal-based vibration control of a wind turbine tower using a small-scale electric drive with MR damper support. *Energies* **2022**, *15*, 9530. [\[CrossRef\]](#)
- GWEC. *Global Offshore Wind Report, 2022*; GWEC Asia Ltd.: Singapore, 2022.

23. Jonkman, J.; Matha, D. A Quantitative Comparison of the Responses of Three Floating Platform Concepts. In Proceedings of the European Offshore Wind 2009 Conference and Exhibition, Stockholm, Sweden, 14–16 September 2009; Conference Paper NREL/CP-500-46726. National Renewable Energy Laboratory: Golden, CO, USA, 2010.
24. Katsaounis, G.M.; Polyzos, S.; Mavrakos, S.A. An Experimental Study of the Hydrodynamic Behavior of a TLP Platform for a 5MW Wind Turbine with OWC Devices. In Proceedings of the VII International Conference on Computational Methods in Marine Engineering (MARINE 2017), Nantes, France, 15–17 May 2017.
25. Konispoliatis, D.; Katsaounis, G.M.; Manolas, D.; Soukissian, T.; Polyzos, S.; Mazarakos, T.P.; Voutsinas, S.G.; Mavrakos, S.A. REFOS: A Renewable Energy Multi-Purpose Floating Offshore System. *Energies* **2021**, *14*, 3126. [[CrossRef](#)]
26. Jonkman, J.; Butterfield, S.; Musial, W.; Scott, G. *Definition of a 5-MW Reference Wind Turbine for Offshore System Development*; Technical Report NREL/TP-500-38060; National Renewable Energy Laboratory: Golden, CO, USA, 2009.
27. Bir, G.; Jonkman, J. Modal Dynamics of Large Wind Turbines with Different Support Structures. In Proceedings of the International Conference on Offshore Mechanics and Arctic Engineering, Estoril, Portugal, 15–20 June 2008; Conference Paper NREL/CP-500-43045. National Renewable Energy Laboratory: Golden, CO, USA, 2008.
28. Stewart, G.; Lackner, M. Offshore Wind Turbine Load Reduction Employing Optimal Passive Tuned Mass Damping Systems. *IEEE Trans. Control Syst. Technol.* **2013**, *21*, 1090–1104. [[CrossRef](#)]
29. Park, S.; Lackner, M.A.; Cross-Whiter, J.; Tsouroukdissian, A.R.; La Cava, W. An investigation of passive and semi-active tuned mass dampers for a tension leg platform floating offshore wind turbine in ULS conditions. In Proceedings of the ASME 2016 35th International Conference on Ocean, Offshore and Arctic Engineering, Busan, Republic of Korea, 19–24 June 2016.
30. Park, S.; Lackner, M.A.; Pourazarm, P.; Tsouroukdissian, A.R.; Cross-Whiter, J. An investigation on the impacts of passive and semiactive structural control on a fixed bottom and a floating offshore wind turbine. *Wind Energy* **2019**, *22*, 1451–1471. [[CrossRef](#)]
31. Asareh, M.A.; Schonberg, W.; Volz, J. Fragility Analysis of a 5-MW NREL Wind Turbine Considering Aero-Elastic and Seismic Interaction Using Finite Element Method. *Finite Elem. Anal. Des.* **2016**, *120*, 57–67. [[CrossRef](#)]
32. Hu, Y.; He, E. Active structural control of a floating wind turbine with a stroke-limited hybrid mass damper. *J. Sound Vib.* **2017**, *410*, 447–472. [[CrossRef](#)]
33. Martynowicz, P.; Santos, M. Structural vibration control of NREL 5.0 MW FOWT using optimal-based MR tuned vibration absorber. In Proceedings of the 21st IFAC World Congress, Berlin, Germany, 11–17 July 2020.
34. Vardaroglu, M.; Gao, Z.; Avossa, A.M.; Ricciardelli, F. Validation of a TLP wind turbine numerical model against model-scale tests under regular and irregular waves. *Ocean Eng.* **2022**, *256*, 111491. [[CrossRef](#)]
35. Madsen, F.J.; Nielsen, T.R.L.; Kim, T.; Bredmose, H.; Pegalajar-Jurado, A.; Mikkelsen, R.F.; Lomholt, A.K.; Borg, M.; Mirzaei, M.; Shin, P. Experimental analysis of the scaled DTU10MW TLP floating wind turbine with different control strategies. *Renew. Energy* **2020**, *155*, 330–346. [[CrossRef](#)]
36. Larsen, T.G.; Zhang, Z.; Høgsberg, J. Vibration damping of an offshore wind turbine by optimally calibrated pendulum absorber with shunted electromagnetic transducer. *J. Sound Vib.* **2021**, *505*, 116144. [[CrossRef](#)]
37. Shen, Y.J.; Wang, L.; Yang, S.P.; Gao, G.S. Nonlinear dynamical analysis and parameters optimization of four semi-active on-off dynamic vibration absorbers. *J. Vib. Control* **2013**, *19*, 143–160. [[CrossRef](#)]
38. Hu, Y.; Chen, M.Z.Q.; Li, C. Active structural control for load mitigation of wind turbines via adaptive sliding-mode approach. *J. Frankl. Inst.* **2017**, *354*, 4311–4330. [[CrossRef](#)]
39. Bryson, A.E.; Ho, Y.C. *Applied Optimal Control*; Taylor & Francis: Abingdon, UK, 1975.
40. Shukla, P.; Ghodki, D.; Manjarekar, N.S.; Singru, P.M. A Study of H infinity and H2 synthesis for Active Vibration Control. *IFAC-PapersOnLine* **2016**, *49*, 623–628. [[CrossRef](#)]
41. Itik, M. Optimal control of nonlinear systems with input constraints using linear time varying approximations. *Nonlinear Anal. Model. Control* **2016**, *21*, 400–412. [[CrossRef](#)]
42. Snamina, J.; Martynowicz, P. Prediction of characteristics of wind turbine's tower-nacelle system from investigation of its scaled model. In Proceedings of the 6WCSCM: Sixth World Conference on Structural Control and Monitoring—Proceedings of the 6th Edition of the World Conference of the International Association for Structural Control and Monitoring (IACSM), Barcelona, Spain, 15–17 July 2014.
43. Ioffe, A.D.; Tihomirov, V.M. *Theory of Extremal Problems. Studies in Mathematics and Its Applications*; North-Holland Publishing Company: Amsterdam, The Netherlands, 1979.
44. Länger-Möller, A. Simulation of transient gusts on the NREL 5MW wind turbine using the URANS solver THETA. *Wind Energy Sci.* **2018**, *3*, 461–474. [[CrossRef](#)]
45. Maślanka, M. Optimised semi-active tuned mass damper with acceleration and relative motion feedbacks. *Mech. Syst. Signal Process.* **2019**, *130*, 707–731. [[CrossRef](#)]

Disclaimer/Publisher's Note: The statements, opinions and data contained in all publications are solely those of the individual author(s) and contributor(s) and not of MDPI and/or the editor(s). MDPI and/or the editor(s) disclaim responsibility for any injury to people or property resulting from any ideas, methods, instructions or products referred to in the content.